



TURKGEO

TURKISH JOURNAL OF GEOSCIENCES

e-ISSN 2717-7696

OPEN ACCESS



dergipark.org.tr/tr/pub/turkgeo
turkgeosciences@gmail.com

TURKGEO, June/2021
Volume: 2 - Issue: 1

About The Journal

Turkish Journal of Geosciences is a multi-disciplinary open-access journal aimed to publish peer-reviewed original research and review articles covering all aspects of geosciences. The journal includes a wide scope of information on scientific and technical advances in all areas related to geosciences and indexed in international indices and databases that publish studies on earth sciences.

Aim and Scope

TURKGEO Journal has the following aim and scopes;

Aim of TURKGEO

- TURKGEO aims to promote the theory and practice from the integration of instruments, methodologies, and technologies and their respective uses in the environmental and other natural sciences.
- TURKGEO aims to provide a widely accessible discussion environment that will strengthen and accelerate the exchange of knowledge and experience among scientists, researchers, engineers and other implementers involved in the subject directly or indirectly.

Scope of TURKGEO

- Earth and Environmental Sciences Applications
- Geographic Information Systems
- Remote Sensing
- Photogrammetry
- Geostatistics
- GPS/GNSS
- RADAR/SAR/LIDAR and Laser Scanning
- Spatial Data Infrastructure
- Spatial Decision Support Systems
- Climate Change
- Geology
- Geomorphology
- Hydrogeology
- Geophysics
- Hydrology and Water Resources
- Oceanography

Publishing Frequency

2 issues per year (June-December)

ISSN

2717-7696

WEB

<https://dergipark.org.tr/tr/pub/turkgeo>

Contact

sefa.bilgilioglu@gmail.com / osmanorhan44@gmail.com

EDITOR

Assist. Prof. Dr. Süleyman Sefa BİLGİLİOĞLU

Aksaray University, Faculty of Engineering, Department of Geomatics Engineering /Aksaray/Turkey

ASSOCIATE EDITOR

Assist. Prof. Dr. Osman ORHAN

Mersin University, Institute of Science, Remote Sensing and GIS /Mersin /Turkey

SECTION EDITORS

Assist.Prof. Dr. Bahattin GÜLLÜ, AKSARAY UNIVERSITY
Assist.Prof. Dr. Emine BAŞTÜRK, AKSARAY UNIVERSITY
Dr. Mehmet MESUTOĞLU, KONYA TECHNICAL UNIVERSITY

EDITORIAL BOARD

Prof. Dr. Abdurrahman EYMEN, Erciyes University
Prof. Dr. Alper BABA, Izmir Institute Of Technology
Prof. Dr. C. Serdar BAYARI, Hacettepe University
Prof. Dr. Fatih İŞCAN, Konya Technical University
Prof. Dr. Fevzi KARSLI, Karadeniz Technical University
Prof. Dr. Füsün BALIK ŞANLI, Yıldız Technical University
Prof. Dr. Hakan KARABÖRK, Konya Technical University
Prof. Dr. Hediye ERDOĞAN, Aksaray University
Prof. Dr. Mehmet ÇELİK, Ankara University
Prof. Dr. Murat YAKAR, Mersin University
Prof. Dr. Mustafa YANALAK, ISTANBUL TECHNICAL UNIVERSITY
Prof. Dr. Nebiye MUSAOĞLU, Istanbul Technical University
Prof. Dr. Niyazi ARSLAN, Cukurova University
Prof. Dr. Orhan AKYILMAZ, Istanbul Technical University
Prof. Dr. Reha Metin ALKAN, Istanbul Technical University
Assoc. Prof. Dr. Fatih POYRAZ, Cumhuriyet University
Assoc. Prof. Dr. Hakan YAVAŞOĞLU, Istanbul Technical University
Assoc. Prof. Dr. Himmet KARAMAN, Istanbul Technical University
Assoc. Prof. Dr. Hüseyin KARAKUŞ, Dumlupınar University
Assoc. Prof. Dr. İbrahim TIRYAKIOĞLU, Afyon Kocatepe University
Assoc. Prof. Dr. Mustafa EL-RAWY, Shaqra University
Assoc. Prof. Dr. Serkan DOĞANALP, Konya Technical University
Assoc. Prof. Dr. Tekin SUSAM, Gazi Osman Pasa University
Assoc. Prof. Dr. Uğur AVDAN, Eskisehir Technical University
Assoc. Prof. Dr. Zaide DURAN, Istanbul Technical University
Assist. Prof. Dr. Aydan YAMAN, Aksaray University
Assist. Prof. Dr. Bahattin GÜLLÜ, Aksaray University
Assist. Prof. Dr. Can İBAN, Mersin University
Assist. Prof. Dr. Erkan YILMAZER, Aksaray University
Assist. Prof. Dr. Emine BAŞTÜRK, Aksaray University
Assist. Prof. Dr. Esra GÜRBÜZ, Aksaray University
Assist. Prof. Dr. Kamil KARATAŞ, Aksaray University
Assist. Prof. Dr. Nizar POLAT, Harran University
Assist. Prof. Dr. Özlem GÜLLÜ, Aksaray University
Assist. Prof. Dr. Resul ÇÖMERT, Gumushane University
Assist. Prof. Dr. Sefa YALVAÇ, Gumushane University
Assist. Prof. Dr. Zehra YIGIT AVDAN, Eskisehir Technical University
Dr. Burak Ömer SARAÇOĞLU
Dr. Fabiana CALO, CNR IREA
Dr. Homayoun MOGHIMI, Payame Noor University
Dr. Kaan KALKAN, TUBITAK-UZAY Space Technologies Research Institute
Dr. Syed Mobasher AFTAB, University Of Balochistan

ADVISORY BOARD

Prof. Dr. Bahadır AKTUĞ, Ankara University
Prof. Dr. Dursun Zafer ŞEKER, Istanbul Technical University
Prof. Dr. Hacı Murat YILMAZ, Aksaray University
Prof. Dr. Hatim ELHATİP, Aksaray University
Prof. Dr. Haluk ÖZENER, Bogazici University
Prof. Dr. Mustafa AFŞİN, Aksaray University
Prof. Dr. Mustafa IŞIK, Aksaray University
Prof. Dr. Yusuf Kağan KADIOĞLU, Ankara University

TECHNICAL STAFF










Ahmet Tarık TORUN, Aksaray University
Burhan Baha BİLGİLİOĞLU, Gumushane University
Cemil GEZGIN, Aksaray University
Halil İbrahim GÜNDÜZ, Aksaray University
Ozan ÖZTÜRK, ISTANBUL Technical University
Mustafa Haydar TERZİ, Aksaray University

Contents

Research Articles;

Page	Article Titles and Authors
1-	<i>Groundwater Sustainability and The Divergence of Rock Types in a Typical Crystalline Basement Complex Region, Southwestern Nigeria</i> Bawallah Musa ADESOLA, Adiat Kola ABDUL-NAFIU, Akinlalu Ayokunle ADEWALE, Ilugbo Stephen OLUBUSOLA, Akinluyi Francis OMOWONUOLA, Benjamin Odey OMANG, Oyedele Akintunde AKINOLA, Omosuyi Oluwole GREGORY, Aigbedion ISAAC
12-	<i>Numerical Evaluation of the Performance for a Different Structural System Against Seismic Movements in Multi-Storey Reinforced Concrete Buildings</i> Miraç MESUTOĞLU, Hatip TOK
18-	<i>Thermal Anomaly Detection of Industrial Zones with MNF and ICA</i> Enis ARSLAN
27-	<i>Unmanned Aerial Vehicle Data Documentation of Cultural Heritage Availability: 1001 Church</i> Mehmet Samet SUCU, Hacı Murat YILMAZ
33-	<i>Investigation of Disasters with Different InSAR Methods</i> Bekir GÜNDOĞDU, Hediye ERDOĞAN, Osman OKTAR

Groundwater Sustainability and The Divergence of Rock Types in a Typical Crystalline Basement Complex Region, Southwestern Nigeria

Bawallah Musa ADESOLA¹, Adiat Kola ABDUL-NAFIU¹, Akinlalu Ayokunle ADEWALE¹, Ilugbo Stephen OLUBUSOLA *¹, Akinluyi Francis OMOWONUOLA², Benjamin Odey OMANG³, Oyedele Akintunde AKINOLA⁴, Omosuyi Oluwole GREGORY¹, Aigbedion ISAAC⁵

¹Department of Applied Geophysics, Federal University of Technology, Akure, Nigeria

²Department of Remote Sensing and GIS, Federal University of Technology Akure, Ondo State, Nigeria

³Department of Geology, University of Calabar, Cross River State, Nigeria

⁴Department of Physics, Ekiti State University, Ado-Ekiti, Nigeria

⁵Department of Physics, Ambrose Alli University, Ekpoma, Nigeria

Keywords

Coefficient anisotropy
Longitudinal conductance
Transverse resistance
Rock types
Groundwater yield

ABSTRACT

This study investigates the relationship among the various types of rock within the basement complex region and their possible yield in term of groundwater productivity. Four different rock types were considered at various locations in Akure metropolis. Electrical resistivity method was adopted using horizontal profiling utilizing Wenner array as well as Vertical Electrical Sounding (VES) technique using Schlumberger configuration. The horizontal profiling technique was used to determine areas characterized by structural features associated with weak zones that may be diagnostics of cracks, joints, fractures or highly weathered geologic material, while VES was used as a follow up to identified weak zones as a confirmatory test as well as delineation of layer stratification and geologic materials associated with layer parameters that maybe applicable for groundwater occurrence. The results derived from geoelectric parameters were used to determine the second order parameters (Dar-Zarrouk) for groundwater productivity modeling. The finding reflects the various yield capacity of the different rock types that were considered for this study and without prejudice to fracture/thick weathered basement.

1. INTRODUCTION

The problem of public water supply especially for sustainable industrial and domestic water supply has become a matter of major concern to all (Ozegin et al., 2019). This is against the background of mass neglect of public utilities by successive government since the early 1980's, as result of corruption and lack of sustainable vision, which has prompted private efforts directed at water sustainability in form of boreholes (Ilugbo et al., 2019). However, due to rapid population growth and human development, the land use for building and industrial development is on the increase. This has becomes a major challenge within the basement complex region

especially where the areas characterized by thick overburden has been subjected to other applications rather than groundwater development, thereby exposing the populate to the development, exploration and exploitation of groundwater by a way of harnessing water from structural features associated with crack, fault, fractures or highly weathered materials with little or no reasonable overburden thickness (Olorunfemi et al., 1991; Ilugbo and Adebisi, 2017; Babatunde et al., 2018). Delineation of zones of major anomaly/weak zones characterizing of high water bearing zones for sustainable water development in a typical complex crystalline basement rock terrain such as that of Akure and its environment southwestern Nigeria,

* Corresponding Author

Cite this article

(mbawallah@futa.edu.ng) ORCID ID 0000-0002-7862-613X
(Kanadiat@futa.edu.ng) ORCID ID 0000-0002-2261-4543
(aakinlalu@futa.edu.ng) ORCID ID 0000-0002-6165-760X
(bussytex4peace44@gmail.com) ORCID ID 0000-0002-1001-4815
(fakinluyi@futa.edu.ng) ORCID ID 0000-0003-4278-4926
(oobenjami@unical.edu.ng) ORCID ID 0000-0001-9196-3109
(akinkin02@yahoo.com) ORCID ID 0000-0003-4372-276X
(dromosuyi@yahoo.com) ORCID ID 0000-0002-9798-8574
(lsaacaigbedion@yahoo.com) ORCID ID 0000-0002-0969-3451

Adesola, B, Abdul-nafiu, A, Adewale, A, Olubusola S I, Omowonuola, A, Omang, B, Akinola, O, Gregory, O, Isaac, A. (2021). Groundwater Sustainability and the Divergence of Rock Types in a Typical Crystalline Basement Complex Region, Southwestern Nigeria. Turkish Journal of Geosciences, 2 (1), 1-11. DOI: 10.48053/turkgeo.777217

requires a strategic approach that involve more than one geophysical techniques for random sampling (Isogun and Adepelumi, 2014; Ozegin et al., 2019). This is due to the highly localized nature of the water bearing formation/weak zones that may not be identified nor delineated by random sampling techniques using Vertical Electrical Sounding (VES). Identification of these highly localized zones of interest is very essential for the successful groundwater exploration and development (Olubusola et al., 2018). This is more so, that previous efforts at relying on just one technique in groundwater investigation (VES) has often been met by failures of poor results. This is as a result of the complex nature of the various rock types associated with the basement rock types in the region vis-à-vis their varying degree of fracturing, faulting and weathering that require delineation of viable weak zones within a particular locality, using other geophysical techniques before relying on VES for further investigation. As a result of non-availability of electromagnetic, magnetic, gravity and seismic refraction equipments for necessary reconnaissance survey in delineating structures for groundwater exploration and development (Bawallah et al., 2018). Lateral resistivity profiling has been deployed as a viable tool in delineating and mapping geologic structures within a particular location for groundwater exploration in a crystalline basement complex. This calls for ingenuity on the part of the geophysicist to deploy all this professional experience at challenging nature and getting the best in an attempt at minimizing the problem of sustainable water supply. Therefore, this study has been directed at studying different rock types, with the prospect of finding water in a basement complex environment with little or no reasonable overburden thickness in terms of geology of the environment, as was the case in this study location within the basement complex region of Akure and its environs with a view to determining its groundwater prospect, sustainability and possible yields.

2. METHOD

2.1. Site Description and Geology of the Study Area

The study area falls within Akure metropolis, Ondo State, southwestern Nigeria. It lies between latitude 798000N to 810000N and longitude 734700E to 746200E (Figure 1). It is well accessible through several road networks within and around the study area. The study area can be described as moderately undulating and the drainage pattern is dendritic. The climate of the area consists of two seasons; dry season (November to March) and wet season (April to October) seasons. The mean annual rainfall ranges between 1000 and 1500 mm. The mean annual temperature distribution is 27°C (Iloje, 1981). The study area is underlain by rocks of the precambrian basement complex of

southwestern Nigeria (Rahaman, 1989). The geological mapping and other related studies of the area around the Akure metropolis have been carried out by several workers amongst who are (Olawaju, 1988; Owoyemi, 1996; Odeyemi et al., 1999; Slomczyńska and Slomczyński 2004; Aluko, 2008; Adebisi et al., 2018). The area around the Akure metropolis is underlain by eight petrological units of the basement complex of southwestern Nigeria identified by (Rahaman, 1988) and also described by (Olawaju, 1988; Rahaman, 1988; Aluko, 2008). These are the Migmatite-Gneiss, Quartzite, Charnockitic, biotite gneiss, migmatite gneiss, peltic schist, granite gneiss and porphyritic granite (Figure 2).

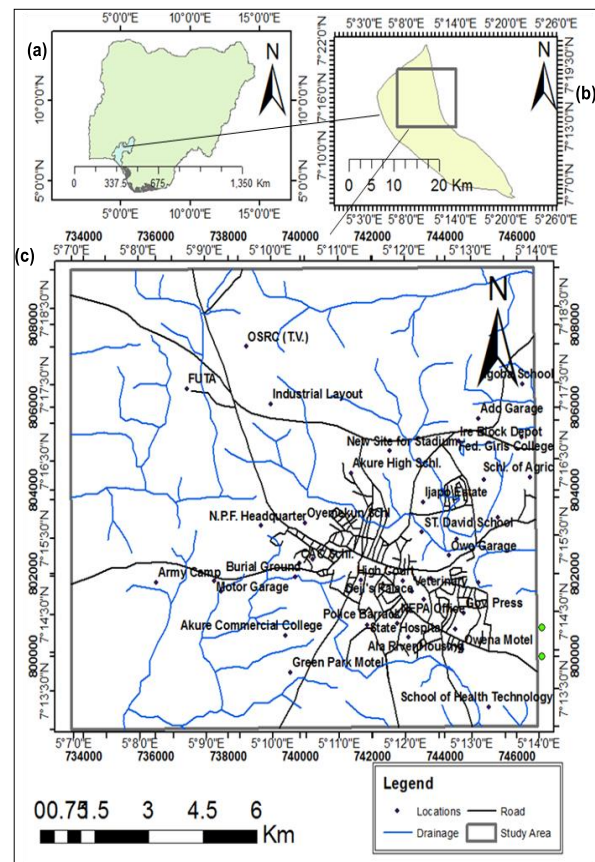


Figure 1. (a) Map of Nigeria and Ondo state showing Akure metropolis, (b) Map of Akure metropolis showing the location area (c) Location map showing the study area

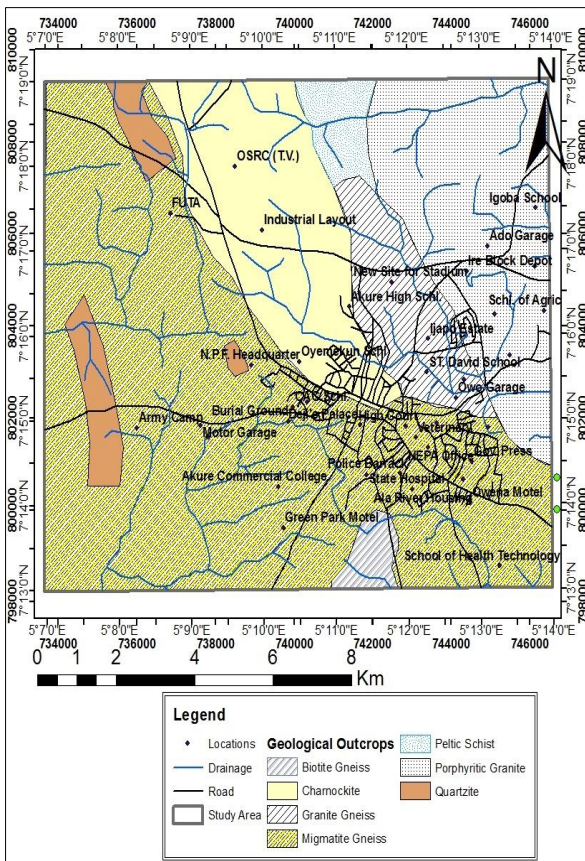


Figure 2. Geological map of the study area

2.2. Research Methodology

Nine locations were used for this research in Akure, Ondo State, southwestern Nigeria, with traverses established in an approximate E-W direction with length variation from 50 m to 200 m depending on available space in each of the location (Figure 3). The electrical resistivity method utilized the VES and the horizontal profiling techniques. The horizontal profiling utilizing Wenner electrode configuration of station separations and electrode spacing of 20 m with electrode movement of 5 m were used for the traverses. Resistivity values were obtained by taking readings using the omega resistivity meter. The horizontal profiling data were plotted on excel work sheet to identified the zones of contrast/anomaly. VES were carried out on points of resistivity contrast/major anomaly irrespective of weather the resistivity at any specific location is generally low or high. The VES data were presented as sounding curves, which are plots of apparent resistivity values against electrode separation (AB/2) on bilogarithmic paper resulting in a VES curve. The VES curve showed the change of resistivity with depth, since the effective penetration increases with increasing electrode spacing. The interpretation of the VES curve is both qualitative and quantitative. The qualitative interpretation involved visual inspection of the sounding curves while the quantitative interpretation utilized partial curve matching technique using 2-layer master

curve which was later refined by a computer iteration technique resist version (Vander, 2004) that is based upon an algorithm of (Ghosh, 1971). The quantitatively interpreted sounding curves gave results as geoelectric parameters (that is, layer resistivity and layer thickness). The Dar-Zarrouk parameters are obtained from the first order parameters (geoelectric parameters) which are total longitudinal unit conductance (S), total transverse unit resistance (T) and coefficient of anisotropy (λ) using below mathematical expressions. The product of total transverse resistance and coefficient of anisotropy was used to determine the groundwater yield for each outcrop.

$$S = \sum_{i=1}^N \frac{h_i}{\rho_i} \quad (\Omega - 1 \text{ or Siemens}) \quad (1)$$

and

$$T = \sum_{i=1}^N \rho_i h_i \quad (\Omega m^2) \quad (2)$$

When a number of layers with thicknesses of $h_1, h_2, h_3,$ transverse resistances of $T_1, T_2, T_3, \dots,$ and conductance of $S_1, S_2, S_3,$ respectively, are involved in a geoelectrical section, their total longitudinal conductance (S) or total transverse resistance (T) may have to be considered (Sabnavis and Patangay, 1998) and are given by:

$$S = S_1 + S_2 + S_3 + \dots \dots \dots \text{Where } S_1 = \frac{h_1}{\rho_1} \quad (3)$$

and

$$T = T_1 + T_2 + T_3 + \dots \dots \text{Where } T_1 = h_1 \rho_1 \quad (4)$$

If the total thickness of the layers in the geoelectrical section considered is H, then the average longitudinal resistivity ρ_t is given by:

$$\rho_t = \sum_{i=1}^N \frac{h_i}{S_i} \quad (5)$$

and the average transverse resistance ρ_t is given by:

$$\rho_t = \sum_{i=1}^N \frac{T_i}{h_i} \quad (6)$$

ρ_t is always greater than ρ_l . Therefore, the entire section will thus be always anisotropic (Singhal and Niwas 1981) with regard to electrical resistivity. The coefficient of electrical anisotropy is defined as;

$$\lambda = \sqrt{\frac{\rho_t}{\rho_l}} \quad (7)$$

Also the groundwater yield, Y , is a function of the volume of the accumulated groundwater and the permeability of an aquifer. This is influenced, controlled and dependent on the product of coefficient of anisotropy (λ) and total transverse resistance (T) (Bawallah et al., 2018; Olubusola et al., 2018). The relationship is shown as:

$$Y = \lambda \times T \quad (8)$$

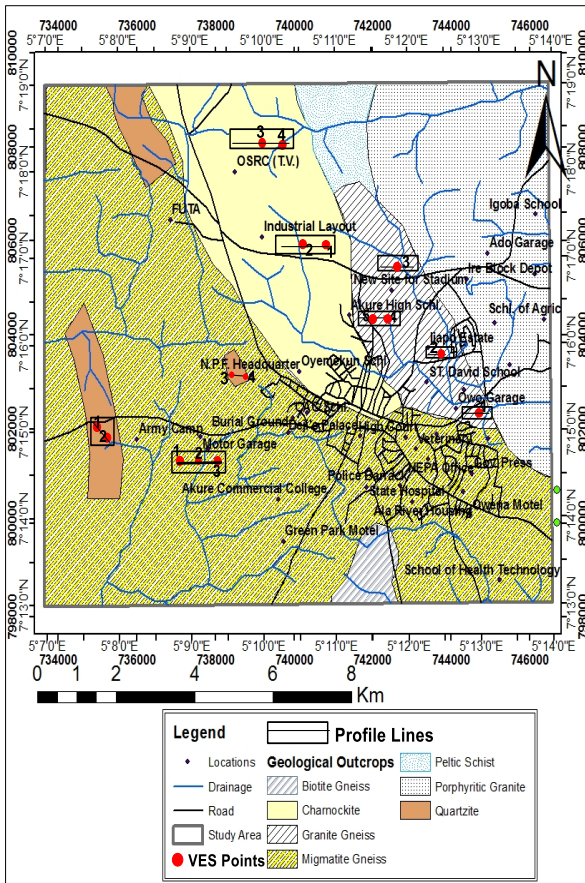


Figure 3. Data acquisitions map of the study area

3. RESULTS and DISCUSSION

These approaches were deployed with intention to pin down the zones of weakness that could be identified as characteristics of fracture, joint, cracks or highly weathered basement complex materials. This is against the background that all the areas of study investigated for the purpose of this research are characterized majorly by shallow overburden and many a time with very little or no overburden material with exposed fresh basement rock materials dotting or been noticed within the surrounding of the study location. Therefore, the challenge here is to locate groundwater not from thick overburden but within the domain of fracture, fault or highly weathered crystalline basement rock material. Hence, the vertical electrical soundings carried out were done as follow up to identified weak zones capable of generating groundwater. However, a control measure was also adopted by sounding

points that were not identified as weak zones, randomly, as a control for a better understanding of the various crystalline formation to test the effectiveness of the two techniques that were adopted for this study, hence the tables and the subsequent plots are discussed as follow.

3.1. Migmatite Gneiss Rock

Figure 4 showed the outcome of horizontal profiling on migmatite gneiss outcrops. The points of resistivity contrasts diagnostic of zones of geological weakness were observed at 10 m, 40 m and 80 m. These points were further investigated using VES to be able to characterize these points in terms of lithological settings/layers characterization and overburden thickness. From table 1, three VES were carried out at this location. Two of the VES were carry out based on result from Wenner profiling, while the third was carried out randomly as a control to established the effectiveness of Wenner profiling technique in identifying proactive weak zone using gradient approach in a difficult basement complex environment coupled with little or no overburden materials from the result obtained, the most promising point on the profile was located at distance of 15 m. The results obtained from the VES was used to determined the second order Dar-Zarrouk parameters, the result from the VES1 has total longitudinal conductance of $0.103092 \Omega^{-1}$, total transverse resistance value of $65787.5 \Omega m^{-2}$ and coefficient of anisotropy (λ) of 1.647082 from which the groundwater yield was determined from the product of total transverse resistance and coefficient of anisotropy (T and λ) to be 108,357.4 which is a reflection of the groundwater yield capacity of that point. A similar approach was adopted for the second and third VES that were randomly investigated to identify fairly weak zone from Wenner profiling. The findings reveal that the groundwater yield for these points was obtained to be 4401.119 and 26512.6 yield capacity for VES2 and VES3.

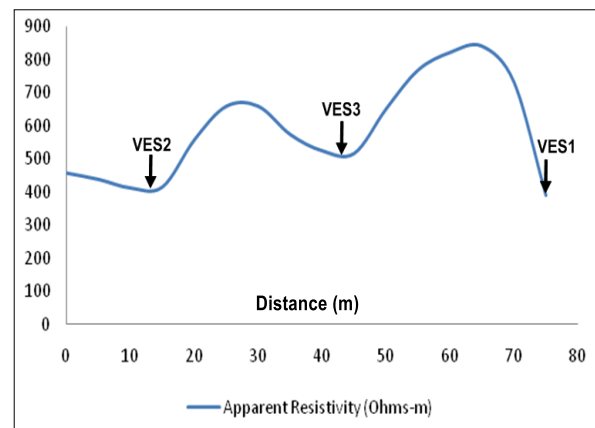


Figure 4. Horizontal profiling along ondo road

Table 1. Dar-Zarrouk parameters and groundwater yield of migmatite gneiss

Migmatite Gneiss	Total Longitudinal Conductance (S) (Ω^{-1})	Total Traverse Resistance (T) (Ωm^2)	Coefficient of Anisotropy (λ)	Groundwater Yield ($T*\lambda$)	Remarks
VES1	0.103092	65787.5	1.647082	108357.4	Thin weathered layer/Fracture extent
VES2	0.063207	3553.4	1.238566	4401.119	Thin weathered layer/Fracture extent
VES3	0.082704	24658.1	1.075208	26512.6	Thick weathered layer/Fracture extent

3.2. Charnockite Rock

Figure 5 was obtained from measurement carried out across charnockite dominated environment along industrial layout. The profile exhibited generally how resistivity contrasts of 120 Ωm . Therefore, considering the inherent nature of charnockite which weathered into clay, and the intrinsic properties of clay in terms of water yield capacity, zone of high resistivity contrasts were considered for VES to be able to characterize the area in terms of layer formations/stratification and bedrock configuration for groundwater yield consideration. Another study was carried out on charnockite dominated environment along Orita Obelle area of Akure (Figure 6). The results show low resistivity throughout the profile reflecting on the clayey nature of the formation emanating from the weathering product of charnockite except between zero to 10 m where the resistivity value is relatively high. Therefore, for the purpose of groundwater yield, the zone of moderately high resistivity contrasts and moderately low resistivity contrasts were considered for further investigation using VES. The information obtained from this location indicated that; for the major weak zone (VES1), the yield parameter obtained from Dar-Zarrouk parameters where total longitudinal conductance has a value of 0.238845 Ω^{-1} and total transverse resistance of 13488.9 Ωm^2 with coefficient of anisotropy of 1.42257. The groundwater yield capacity was determined from the product of total transverse resistance and coefficient of anisotropy (T and λ) as 19188.9 yield capacity. A similar process was adopted for VES2, VES3 and VES4 with their yield rating obtained as 16376.38, 14118.55 and 1261.768 yield capacity (Table 2), all of which were

considered as controlled except for VES1 which was recommended for drilling base on its yield parameter rating.

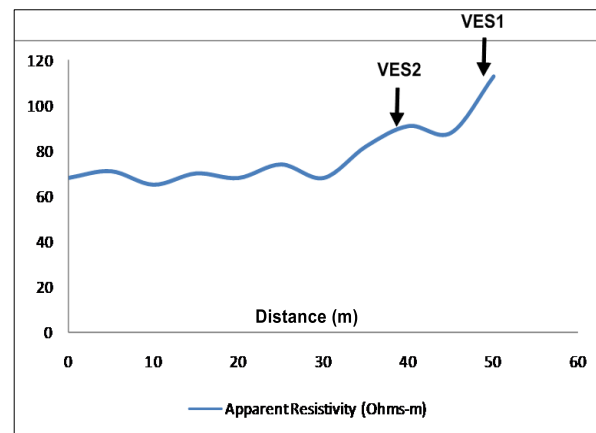


Figure 5. Horizontal profiling along industrial layout

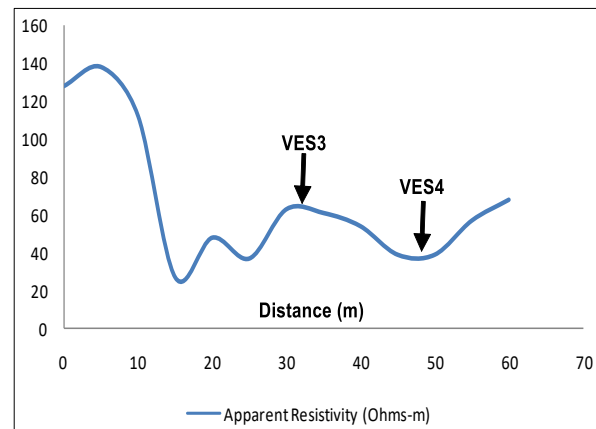


Figure 6. Horizontal profiling along orita obele

Table 2. Dar-Zarrouk parameters and groundwater yield of charnockite

Charnockite	Total Longitudinal Conductance (S) (Ω^{-1})	Total Traverse Resistance (T) (Ωm^2)	Coefficient of Anisotropy (λ)	Groundwater Yield ($T*\lambda$)	Remarks
VES1	0.238845	13488.9	1.42257	19188.9	Thick weathered layer/Fracture extent
VES2	0.140923	6886.5	2.37804	16376.38	Fairly thick weathered layer/Fracture extent
VES3	0.468766	7356.8	1.919116	14118.55	Fairly thick weathered layer/Fracture extent
VES4	0.68402	663.4	1.901972	1261.768	Very thin weathered layer/Fracture extent

3.3. Granite Gneiss Rock

Figure 7 showed that the study area was characterized by high resistivity with lowest being 240 Ω m at the beginning of the measurement point, and continue to increase even beyond 400 Ω m towards the end of the profile indicating the nature and its geological settings and structural disposition from the beginning to the end of the profile. A follow up investigation was carried out at the point considered as the weak zone (lowest resistivity contrast) for further consideration using VES for the purpose of groundwater potential yield. Another investigation was carried out at Ijapo area of Akure metropolis across the same rock types (Granite Gneiss) with rock exposure and low lying outcrops (Figure 8). The profile covered a distance of 50 m while the weak zone delineated resulting from resistivity contrast was located at 10 m. Figure 9 was carried out on the same outcrop along Araromi area of Akure, following the same principle and approach which covered a distance of 50 m. On this location, the zone of major resistivity contrasts anomaly was identified at 30 m upon which further investigation was carried out in order to determine its hydrogeological parameters/geological setting using VES. Furthermore, this research effort was extended to another location along Akure high school area of Akure (Figure 10), where measurement obtained from this area shows two anomalous zones (zones of weakness). These zones were further investigated for lithological setting, geoelectric parameters and bedrock depositions to determine the groundwater potential and yield. The VES was carried out on the identify major weak zones obtained from horizontal profiling to delineate major structural feature, that could be diagnostic of fracture, fault or highly weathered material that could accumulate groundwater exploration and development. In all the five (5) point for the purpose of control and better understanding of the geology and effective correlation of events. The result obtained using the second order parameters (Dar-Zarrouk), indicated a groundwater yield maximum of 8125.562, 11472.65, 15748.28, 5325.984 and 4174.991 for VES1, VES2, VES3, VES4 and VES5 (Table 3). Whereas, all these yield parameters are not reasonable enough to allow groundwater developing, thereby reflecting the importance of narrowing down point of interest with horizontal profiling, as none of these investigated VES points can support borehole and groundwater exploration and development in term of water yield parameters. Justifying the importance's of lateral resistivity profiling technique with VES as a major tool in identifying weak zones in a typical crystalline basement complex region.

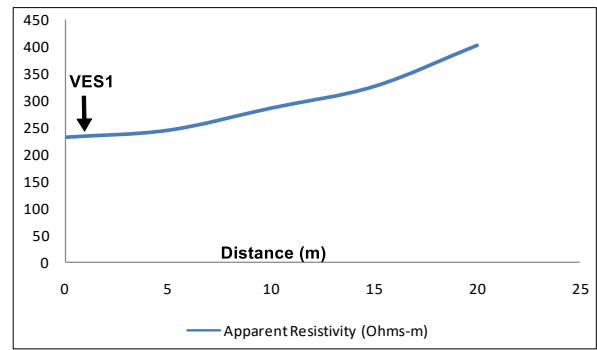


Figure 7. Horizontal profiling along owo garage

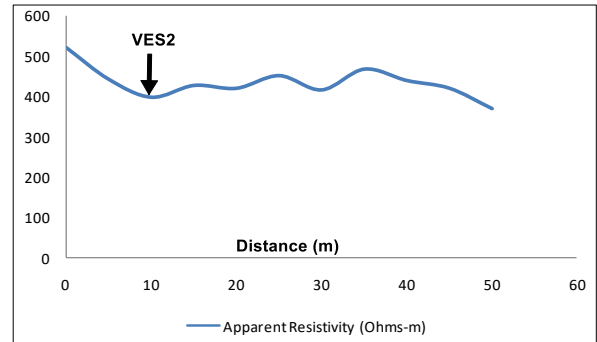


Figure 8. Horizontal profiling along Ijapo estate

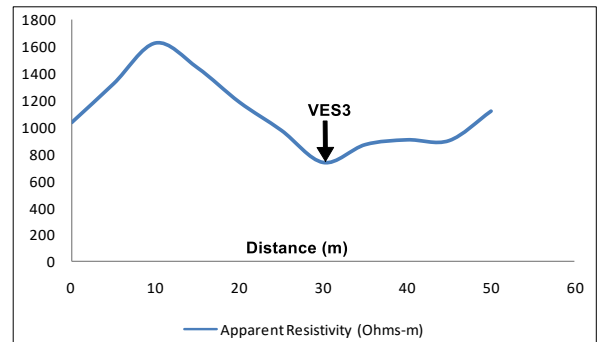


Figure 9. Horizontal profiling along Araromi

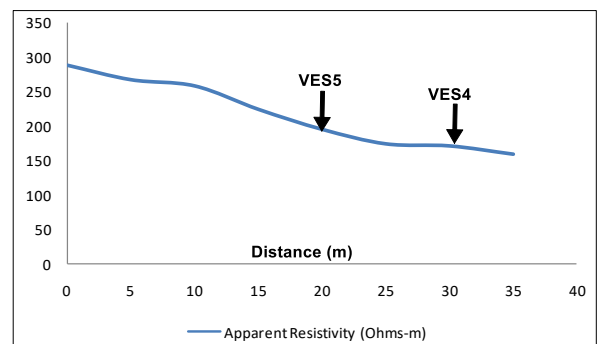


Figure 10. Horizontal profiling along Akure high school

Table 3. Dar-Zarrouk parameters and groundwater yield of granite gneiss

Granite Gneiss	Total Longitudinal Conductance (S) (Ω^{-1})	Total Traverse Resistance (T) (Ωm^2)	Coefficient of Anisotropy (λ)	Groundwater Yield ($T*\lambda$)	Remarks
VES1	0.142428	5872.2	1.383734	8125.562	Very thin weathered layer
VES2	0.064273	8461.6	1.355848	11472.65	fairly thin weathered layer/Fracture extent
VES3	0.097934	13450.9	1.170797	15748.28	fairly thin weathered layer/Fracture extent
VES4	0.130881	4528.5	1.176103	5325.984	very thin weathered layer/Fracture extent
VES5	0.042053	3687.8	1.132109	4174.991	very thin weathered layer/Fracture extent

3.4. Quartzite Rock

Figure 11 showed the outcome of the horizontal profiling along quartzite outcrops and two major zones of weakness were observed at 30 and 35 m which area diagnostic of fracture/fault, cracks/joints or high weathered geologic material which is relevant to groundwater potential yield evaluation. The results obtained at lafe environment along former police headquarter within the Akure metropolis (Figure 12). A similar procedure was carried out to obtained relevant information

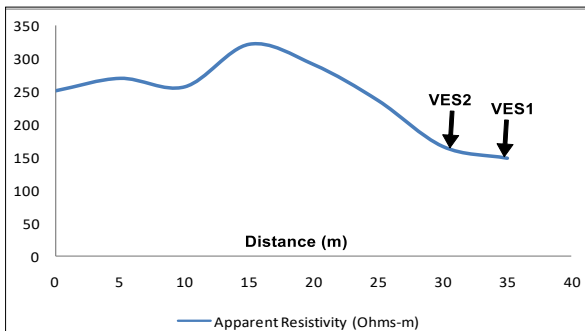


Figure 11. Horizontal profiling along army barrack

necessary to determine the hydrogeological settings and groundwater yield parameters. The zones of weakness were further considered using VES. The location was characterized as quartzite ridge with exposed outcrops of quartzite dotting the entire study area. The groundwater yield parameters obtained were; 5064.894, 1160.35, 17559.38 and 27048.61 for VES1, VES2, VES3 and VES4 (Table 4). The result obtained from lateral resistivity profiling correlated effectively with VES in terms of weak zones.

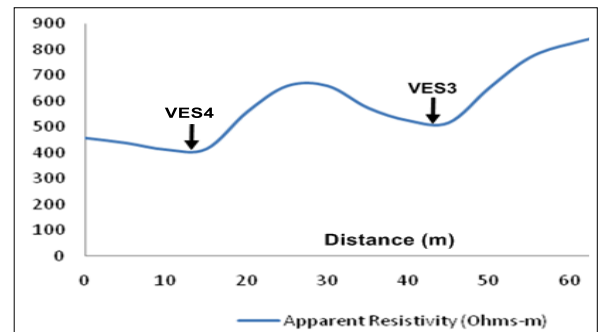


Figure 12. Horizontal profiling along NPF headquarter

Table 4. Dar-Zarrouk parameters and groundwater yield of quartzite

Quartzite	Total Longitudinal Conductance (S) (Ω^{-1})	Total Traverse Resistance (T) (Ωm^2)	Coefficient of Anisotropy (λ)	Groundwater Yield ($T*\lambda$)	Remarks
VES1	0.285939	4245	1.193143	5064.894	very thin weathered layer/Fracture extent
VES2	0.027263	10901.6	1.064188	11601.35	fairly thin weathered layer/Fracture extent
VES3	0.008572	16915.2	1.038083	17559.38	moderately thick weathered layer/Fracture extent
VES4	0.003182	26508	1.020394	27048.61	thick weathered layer/Fracture extent

3.5. Correlation of Results

3.5.1. Total longitudinal conductance

For better understanding of the yield parameters of the different rock types (Granite gneiss, Migmatite gneiss, Quartzite and charnockite) that were found in the investigated locations. The

results obtained were correlated in terms of their various total longitudinal conductance (Ω^{-1}) (Figure 13). Colour separation was used to indicate the performance of each of the outcrops which are very important indicators in terms of groundwater yield. This graph shows that the lower the total longitudinal conductance parameters of a crystalline basement rock, the greater are the prospect

groundwater yield of the outcrops and the higher the total longitudinal conductance parameters of the crystalline basement rocks, the lower the prospect groundwater yield of such rocks.

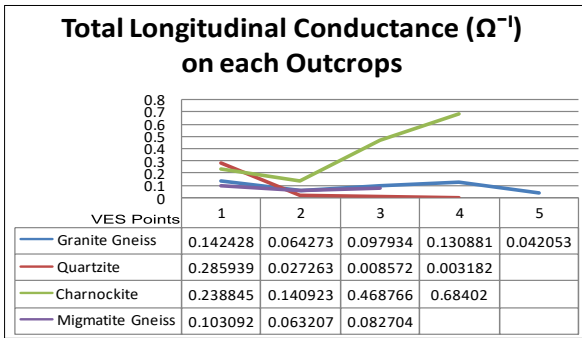


Figure 13. Correlation of total longitudinal conductance across the various rock types within the study area

3.5.2. Total transverse resistance

Figure 14 displays the total transverse resistance of the various outcrops within the study area. It can be further inferred that the higher the total transverse resistance of any crystalline basement rock, the greater is its capacity to yield groundwater and it has an inverse relationship with total longitudinal conductance.

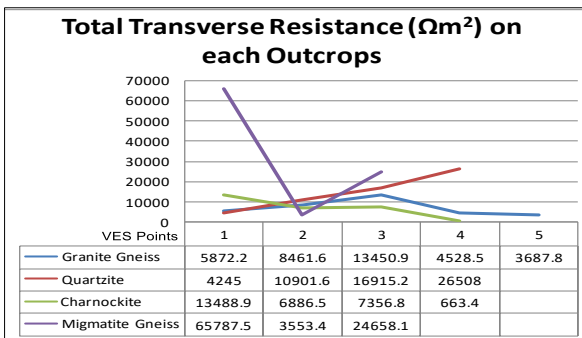


Figure 14. Correlation of total transverse resistance across the various rock types within the study area

3.5.3. Coefficient of anisotropy (λ)

Compact rock at shallow depth increases the coefficient of the anisotropy (Keller and Frischknecht, 1966). Hence, these areas can be associated with low porosity and permeability. The areas with 1.0 and less than 1.5 anisotropy values (high porosity and permeability) are considered as high groundwater potential zones (Rao et al., 2003). The coefficient of anisotropy (λ) has been shown to have the same functional form as permeability anisotropy. Thus, a higher coefficient of anisotropy (λ) implies higher permeability anisotropy. Figure 15 illustrates the coefficient of anisotropy of each

outcrops, it can be inferred that the high the coefficient of anisotropy parameters of any crystalline basement rock, the greater is the prospect for groundwater and also the lower for coefficient of anisotropy, the lower for groundwater prospect without prejudice overburden or weathered layer thickness. The results inferred from coefficient of anisotropy and total longitudinal conductance of each outcrops have a direct relationship.

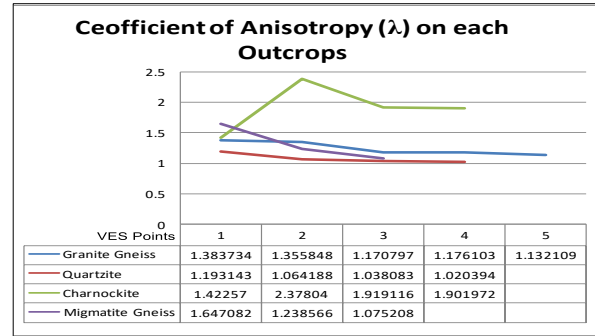


Figure 15. Correlation of coefficient of anisotropy across the various rock types within the study area

3.5.4. Groundwater yield ($T*\lambda$)

The groundwater yield of each outcrop was obtained from the product of total transverse resistance (T) and coefficient of anisotropy (λ) (Bawallah et al., 2018) which was able to establish the productivity of crystalline basement complex in terms of its yield parameters (Figure 16). It further demonstrated the effective correlation of all the approach that was used in the characterization of groundwater yield capacity of crystalline basement rock within the study area. The highest yield results from the various rock types were obtained as 15748.28, 26512.6, 19188.9 and 27048.61 for granite gneiss, migmatite gneiss, charnockite and quartzite. From this analysis it can be inferred that for a typical crystalline basement complex to have better prospect for groundwater, it must base on the various groundwater yield classification (Table 5).

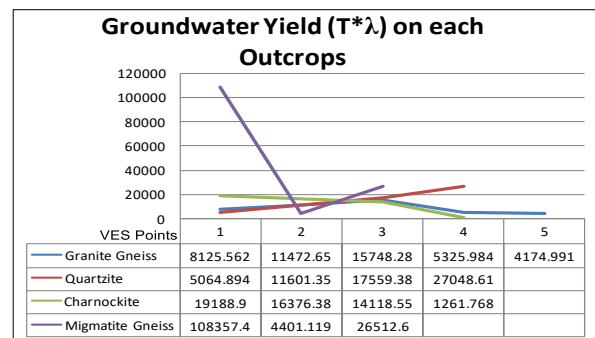


Figure 16. Groundwater yield across the various rock types within the study area

Table 5. Groundwater yield classifications

Rock Types	Groundwater Yield Capacity Value	Classification
Granite Gneiss	Below 8000	No prospect
	8000 – 11000	Low yield
	11000 – 15000	Moderate/Medium Yield
	15000 and above	High Yield
Quartzite	Below 10000	Extremely low yield
	10000 – 15000	Low yield
	15000 – 17000	Moderate yield
	17000 – 20000	High yield
	20000 and above	Very high yield
Charnockite	Below 8000	Very low yield
	8000 – 12000	Low yield
	12000 – 15000	Moderate yield
	15000 – 20000	High yield
Migmatite Gneiss	20000 and above	Very high yield
	Below 5000	Very low yield
	5000 – 10000	Low yield
	10000 – 12000	Moderate yield
	12000 – 15000	High yield
	15000 and above	Very high yield

3.6. Validation/Pumping Test Results

The validation for groundwater taken beyond the domain of using the parameters of precipitation, evaporation and others to determine groundwater yield, but in this study direct measurement of borehole yields was used for the evaluation and rating of groundwater prospect and yield within the study area.

Loction 1: Charnockite Environment

Pumping machine capacity = one horse power
 Overhead tank/reservoir capacity = 1000 litres
 Distance travel by water from borehole to reservoir = 5 meters
 Time taken to fill reservoir = 12 minutes = 12 x 60 = 720 sec

$$\text{Yield} = \frac{1000 \text{ (litres)}}{720 \text{ (sec)}} \times \text{pumping machine capacity} \times \text{distance travel}$$

$$\text{Yield} = \frac{1000}{720} \times 1 \times 5 = 6.94 \text{ litres per sec}$$

Loction 2: Quartzite Environment

Pumping machine capacity = one horse power
 Overhead tank/reservoir capacity = 1500 litres
 Distance travel by water from borehole to reservoir = 30 meters
 Time taken to fill reservoir = 45min = 45 x 60 = 2700 sec

$$\text{Yield} = \frac{1500 \text{ (litres)}}{2700 \text{ (sec)}} \times \text{pumping machine capacity} \times \text{distance travel}$$

$$\text{Yield} = \frac{1500}{2700} \times 1 \times 30 = 16.66 \text{ litres per sec}$$

Loction 3: Migmatite Gneiss environment

Pumping machine capacity = one horse power
 Overhead tank/reservoir capacity = 1500 litres

Distance travel by water from borehole to reservoir = 30 meters

Time taken to fill reservoir = 1hr = 60 x 60 = 3600 sec

$$\text{Yield} = \frac{1500 \text{ (litres)}}{3600 \text{ (sec)}} \times \text{pumping machine capacity} \times \text{distance travel}$$

$$\text{Yield} = \frac{1500}{3600} \times 1 \times 30 = 12.5 \text{ litres per sec}$$

4. CONCLUSION

This study has showed the significance of two techniques in groundwater search in a typical crystalline basement complex with shallow overburden without prejudice to overburden thickness and weathered layer thickness, which may have some degrees of influence on these findings. This study has been able to establish the relationship existing between nature and types of crystalline rock and their groundwater yield/productivity. The highest yield results from the various rock types were obtained as 15748.28, 26512.6, 19188.9 and 27048.61 for granite gneiss, migmatite gneiss, charnockite and quartzite respectively. It can be inferred that for a crystalline basement rocks to be productive in term of groundwater, it is expected to have various groundwater yield classifications. Therefore, it can be infer that without drilling, groundwater productivity and yield can be determined theoretically following these principles. It is of the strong opinion of the authors that it is possible to determine how prolific a borehole would be even before drilling with the adoptions of the approach in this study.

5. DATA AVAILABILITY STATEMENT

The authors confirm that the data supporting the findings of the study are available within the article and its supplementary materials. Authors

have declared that no competing interests exist and the data was not use as an avenue for any litigation but for the advancement of knowledge.

ACKNOWLEDGEMENT

The authors gratefully acknowledge Prof. Aina A.O. and Oladeji J.F for their valuable contribution at improving the quality of this research work.

REFERENCES

- Adebisi, A.D., Ilugbo, S.O., Bamidele, O. E., & Egunjobi, T. (2018). Assessment of aquifer vulnerability using multi-criteria decision analysis around akure industrial estate, Akure, southwestern Nigeria. *Journal of Engineering Research and Reports*, 1-13.
- Aluko, A.B. (2008). Geology of Akure Area Southwestern Nigeria. Unpublished B. Tech. Thesis, Federal University of Technology, Akure, 70.
- Babatunde, A.A., Olubusola, I.S., & Emmanuel, O.F. (2018). Modeling of groundwater potential using Vertical Electrical Sounding (VES) and multi-criterial analysis at omitogun housing estate, Akure, southwestern Nigeria. *Asian Journal of Advanced Research and Reports*, 1-11.
- Bawallah, M.A., Aina, A.O., Ilugbo, S.O., Ozegin, K.O., & Olasunkanmi, K.N. (2018). Evaluation of groundwater yield capacity using Dar-zarrouk parameter of central Kwara State, Southwestern Nigeria. *Asian Journal of Geological Research*, 1-13.
- Ghosh, D.P. (1971). The application of linear filter theory to the direct interpretation of geoelectrical resistivity sounding measurements. *Geophysical prospecting*, 19(2), 192-217.
- Iloje, N.P. (1981). A new geography of Nigeria (New Revised Edition). Longman Group: London, UK. 32-45.
- Ilugbo, S.O., Adebisi, A.D. (2017). Intersection of lineaments for groundwater prospect analysis using satellite remotely sensed and aeromagnetic dataset around Ibodi, Southwestern Nigeria. *International Journal of Physical Sciences*, 12(23), 329-353.
- Ilugbo, S.O., Edunjobi, H.O., Alabi, T.O., Ogabi, A.F., Olomo, K.O., Ojo, O.A. & Adeleke, K.A. (2019). evaluation of groundwater level using combined electrical resistivity log with gamma (Elgg) around Ikeja, Lagos State, Southwestern Nigeria, *Asian Journal of Geological Research*, 1-13.
- Isogun, M.A., Adepelumi, A.A. (2014). The review of seismicity of crustal Mid-Atlantic fracture zone. *International Journal of Scientific and Engineering Research*, 5(10), 1309-1316.
- Keller, G.V., Frischknecht, F.C. (1966). Electrical methods in geophysical prospecting (pp. 179-187), Pergamon Press Inc., Oxford.
- Odeyemi, I.B., Asiwaju-Bello, Y.A., & Anifowose A.Y.B. (1999). Remote sensing fracture characteristics of the Pan African granite batholiths in the Basement Complex of parts of south western Nigeria. *The Journal of Technoscience*, 3, 56-60.
- Olarewaju, V.O. (1988). REE in charnockitic and associated granitic rocks of Ado-Ekiti-Akure, SW Nigeria. *Precambrian Geology of Nigeria, Geological Survey of Nigeria Publication, Kaduna*, 231-239.
- Olorunfemi, M.O., Olarewaju, V.O. & Alade, O. (1991). On the electrical anisotropy and groundwater yield in a basement complex area of SW Nigeria. *Journal of African Earth Sciences*, 12(3):462-472.
- Olubusola, I., Daniel, A., & Oladimeji, O. (2018). Modeling of groundwater yield using GIS and electrical resistivity method in a basement complex Terrain, Southwestern Nigeria. *Journal of Geography, Environment and Earth Science International*, 16(1), 1-17.
- Olubusola, I.S., Adebo, B.A., Oladimeji, O.K., & Ayodele, A. (2018). Application of GIS and multi-criteria decision analysis to geoelectric parameters for modeling of groundwater potential around Ilesha, Southwestern Nigeria. *European Journal of Academic Essays*, 5(5), 105-123.
- Owoyemi, F.B. (1996). A Geologic-Geophysical Investigation of rain-Induced erosional features in Akure metropolis. Unpublished M.Sc. Thesis, Federal University of Technology, Akure. 11-18.
- Ozegin, K.O., Bawallah, M.A., Ilugbo, S.O., Oyedele, A.A., & Oladeji, J.F. (2019). Effect of geodynamic activities on an existing dam: A case study of Ojirami Dam, Southern Nigeria. *Journal of Geoscience and Environment Protection*, 7(9), 200-213.
- Rahaman, M.A. (1988). Recent advances in the study of the basement complex of Nigeria. In Oluyide PO, Mbonu WC, Ogezi AE, Egbuniwe IG, Ajibade AC, Umeji AC. (Eds.). *Precambrian Geology of Nigeria. Geological Survey of Nigeria Special Publication*. 11-41.

Rahaman, M.A. (1989). Review of the basement geology of southwestern Nigeria: In *Geology of Nigeria* (Kogbe CA Ed.). Elizabeth Publishing Co. Nigeria. 41-58.

Rao, P.J., Rao, B.S., Rao, M.J., & Harikrishna, P. (2003). Geo-electrical data analysis to demarcate groundwater pockets and recharge zones in Champavathi River Basin, Vizianagaram District, Andhra Pradesh. *J. Indian Geophys. Union*, 7(2), 105-113.

Sabnavis, M., Patangay, N.S. (1998). Principles and applications of groundwater Geophysics, Publ. by AEG, OU, nHyderabad p 421.

Singhal, D.S., Niwas, S., (1981). Examination of quifertransmissivity from Dar Zarrouk parameters in porous media, *Jour. of Hydrology*, Vol.50 pp 393-399.

Słomczyńska, B., Słomczyński, T. (2004). Physico-chemical and toxicological characteristics of leachates from MSW landfills. *Polish Journal of Environmental Studies*, 13(6), 627-637.

Vander Velpen, B.P.A. (2004). Resist Version 1.0. M.Sc. Research Project, ITC, Delft Netherland”



© Author(s) 2021. This work is distributed under <https://creativecommons.org/licenses/by-sa/4.0/>

Numerical Evaluation of the Performance for a Different Structural System Against Seismic Movements in Multi-Storey Reinforced Concrete Buildings

Miraç Mesutoğlu^{*1}, Hatip Tok¹

¹Kahramanmaraş Sütçü İmam University, Faculty of Engineering and Architecture, Department of Civil Engineering, Kahramanmaraş, Turkey.

Keywords

Braced frame system
Earthquakes
Multi-storey buildings
SAP2000
Shear wall system

ABSTRACT

In recent years, the devastating earthquakes that occurred in many parts of the world have made it even more important the design of earthquake-resistant structures and earthquake performance assessment of existing structures. When innovative systems are examined in building design, it is seen that depending on the developments in recent years, performance-based designs come to the fore in addition to force-based design. This paper provides a new design method's model for multi-storey buildings that can achieve the same resistance against seismic movements by using less concrete and reinforcement using the SAP2000. Modeling studies of the braced frame system used in steel structures for reinforced concrete and multi-storey buildings with different heights was carried out according to 2019 Turkey Building Earthquake Code (TBEC) and Turkish Standard 498 (TS 498). In the modeling studies carried out in reinforced concrete and 20, 30 and 40 storey buildings, the same strength was tried to be obtained with less concrete and reinforcement. As a result of the studies, it has been seen that this new system, which is determined for all models, is an advantageous and performance system in terms of both volume, weight and stabilization compared to reinforced concrete structures with shear wall frame system.

1. INTRODUCTION

Earthquakes that have occurred in different parts of the world from past to present have shown that most buildings are insufficient against large seismic movements. Scientists and researchers have been working to improve the seismic performance of structures for many years (KeerthiGowda and Tajoddeen, 2014).

Earthquakes in the world in recent years have made it necessary to design structures resistant to such a live load, especially to evaluate the earthquake performance of multi-storey buildings (Nath et al., 2018).

Most of the national and international earthquake resistance codes are based on adaptive structures that can absorb and dissipate sizeable amounts of seismic energy through plastic deformations (Phocas and Pamboris, 2009).

Most of the tallest buildings in the world have a steel structure system due to its high strength-to-weight ratio, ease of assembly and field installation, economy of shipping to the site, availability of various strength levels, and wider choice of sections (Kayvani, 2014).

Reinforced concrete structures are especially preferred because the material used is easy to supply and economical. However, a durable structure should be able to withstand the effects of gravity or meteorological forces acting on any structure, regardless of the material used.

Columns, beams, shear walls and floors form the structural system in a building. The structural system that keeps the building up must be in a condition resistant to live loads such as earthquakes (Li, 2010).

There are many studies in the literature on different situations of structural systems. Innovative

* Corresponding Author

Cite this article

^{*}(miracmesutoglu@gmail.com) ORCID ID 0000-0001-8337-7329
(htok@ksu.edu.tr) ORCID ID 0000-0003-0513-0798

Mesutoğlu, M., Tok, H. (2021). Numerical Evaluation of the Performance for a Different Structural System Against Seismic Movements in Multi-Storey Reinforced Concrete Buildings. Turkish Journal of Geosciences, 2(1), 12-17.

“combined with advanced fire protection, corrosion resistance, fabrication and assembly techniques, advanced analytical techniques made possible by the use of computers (Kovacevic and Dzidic, 2018).

In this study, modeling studies of braced frame system used in the steel structures were made for buildings with multi-storey reinforced concrete structure, considering in 2018 Turkey Building Earthquake Code (TBEC) and Turkish Standard 498 (TS 498).

The obtained model results were compared with the shear wall frame system used in reinforced concrete structures in terms of seismic performance.

SAP2000 finite element software was used in modeling studies of this system, which was not used in reinforced concrete structures before in general.

As a result of the modeling studies, it has been tried to obtain better strength results against seismic forces in reinforced concrete and buildings with 20, 30 and 40 floors compared to the shear wall system.

2. METHOD

In the study, in order to show that braced frame systems are more advantageous than shear wall frame systems in terms of performance, shear wall frame and braced frame systems of 3 different building structures (20-30-40 storey) of the same dimensions were modeled in SAP2000 program and their performances were compared.

2.1. Modeling Procedure

While creating the system model, the finite elements representing parts of the structure such as beams, columns, etc., such as structural elements, curtains, walls, flooring, were modeled as shell structural elements.

Elastic or nonlinear joints and springs at the node points or supports, the system model was created using the template systems included in the SAP2000 software.

Model geometry was designed in AutoCAD program for all buildings (20, 30 and 40 storey buildings) and transferred into SAP2000 program.

In SAP 2000, joints are generated automatically by the program. While creating the model geometry, six axes were kept available for all buildings at intervals of 6 meters in + x and + y directions. The floor height is modeled as 3.3 m in all buildings (Figure 1-3).

The buildings must be designed in a way that they can safely carry the fixed and live loads, wind, soil pressure, water, heat and earthquake forces on them. At this stage, it is compulsory to make calculations in accordance with standards and regulations (TBEC, 2018).

In the study, since there is no specific location for the modeled buildings with different heights, analyzes were made using the SAP2000 program standard data. In the model, S_s and S_1 values were determined on the Afad Earthquake Hazard Map

(Figure 4). The ground class for the buildings was taken from the ground study report. Using of the 2018 Turkey Building Earthquake Code, system coefficients of type D and I is entered as an input parameter.

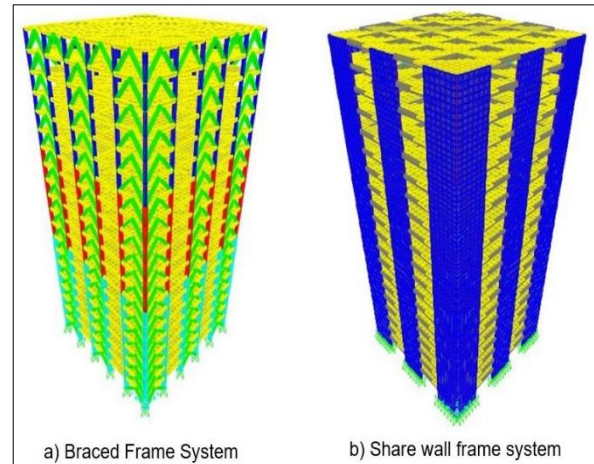


Figure 1. 3D view of shear wall system and braced system model for 20-storey building model

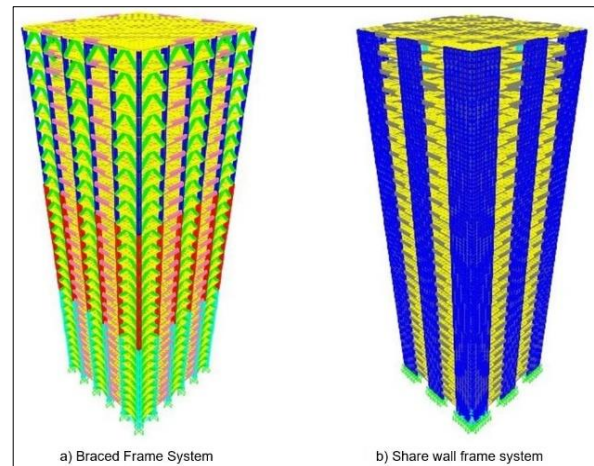


Figure 2. 3D view of shear wall system and braced system model for 30-storey building model

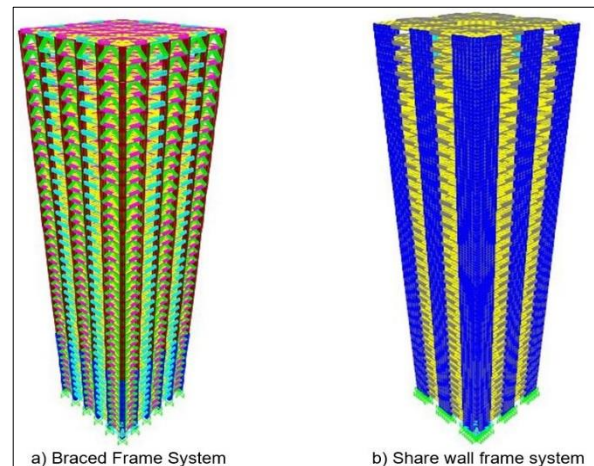


Figure 3. 3D view of shear wall system and braced system model for 40-storey building model

According to TS-498, the characteristic live load is defined as 2 kN / m² on each floor in all building models with different floor heights. The combination of the earthquake effect with other effects is defined in the equations (Equation 1 and equation 2) specified in 2018 TBEC and a total of 64 combinations based on the structural system.

$$G + Q + 0.2S + E_d^{(H)} + 0.3 E_d^{(Z)} \quad (1)$$

$$0.9G + H + E_d^{(H)} - 0.3 E_d^{(Z)} \quad (2)$$

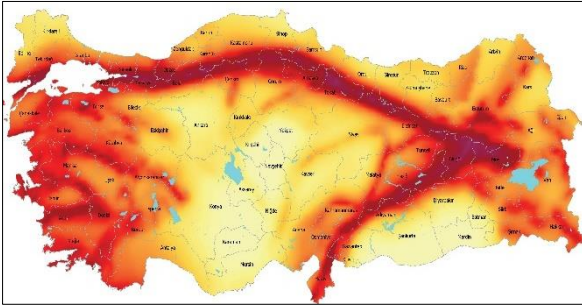


Figure 4. Earthquake hazard map of Turkey (AFAD, 2018)

For all the buildings modeled, linear analysis was chosen as the analysis type in all load classes. In order to obtain the mode shapes of the model and to provide relative displacements, the displacements of the column peaks at the closest position to the center of gravity of the structure were read for each floor.

2.2. Assumptions and Limitations in the Models

Some of the assumptions and limitations of the modeling studies are given below.

The compared buildings in the model studies are assumed to be in the 1st degree earthquake zone. It is assumed that the intended use of the modeled buildings is residential.

Considering to the 2018 Turkey Building Earthquake Code and Turkish Standard-TS498, the following values are used as input parameters in the model analysis (Table 1).

Table 1. Input parameters used in modeling studies

Input Parameters	20-Storey Building	30-Storey Building	40-Storey Building
Building Usage Classification	3	3	3
Earthquake Design Class	1	1	1
Building Importance Factor	1	1	1
Building Height Class	2	1	1
Concrete Class	C35/45	C35/45	C35/45
Steel Class	S420	S420	S420
Floor Load (kN/m ²)	2	2	2

3. RESEARCH RESULTS

The variation of the storey displacement values obtained as a result of the model analysis carried out in the study is presented exemplarily for 20-storey buildings (Table 2 and 3).

According to the 2018 Turkey Earthquake Building Code, the relative floor displacement in other words interstory drift is expressed as the difference of displacements between two consecutive times for a random column or wall (TBEC, 2018).

In the model analysis, the relative floor displacement calculated in columns and shear walls for each storey in the direction of the earthquake were examined. (Table 2 and 3).

Table 2. Displacement and relative floor displacement values for 20-storey building model shear wall frame system.

Floors (Fl.)	Shear Wall Frame System			
	Displacement δ (m)		Relative Floor Displacement $\Delta\delta$ (m)	
	Ex (m)	Ey (m)	Ex (m)	Ey (m)
Fl.-20	0,046935	0,047835	0,002559	0,002616
Fl.-19	0,044376	0,045219	0,002611	0,002667
Fl.-18	0,041765	0,042552	0,002660	0,002716
Fl.-17	0,039105	0,039836	0,002714	0,002771
Fl.-16	0,036391	0,037065	0,002768	0,002825
Fl.-15	0,033623	0,034240	0,002815	0,002873
Fl.-14	0,030808	0,031367	0,002853	0,002910
Fl.-13	0,027955	0,028457	0,002876	0,002931
Fl.-12	0,025079	0,025526	0,002878	0,002934
Fl.-11	0,022201	0,022592	0,002859	0,002913
Fl.-10	0,019342	0,019679	0,002813	0,002864
Fl.-9	0,016529	0,016815	0,002734	0,002784
Fl.-8	0,013795	0,014031	0,002620	0,002667
Fl.-7	0,011175	0,011364	0,002468	0,002511
Fl.-6	0,008707	0,008853	0,002270	0,002309
Fl.-5	0,006437	0,006544	0,002024	0,002059
Fl.-4	0,004413	0,004485	0,001717	0,001745
Fl.-3	0,002696	0,002740	0,001359	0,001381
Fl.-2	0,001337	0,001359	0,000929	0,000945
Fl.-1	0,000408	0,000414	0,000408	0,000414

Table 3. Displacement and relative floor displacement values for 20-storey building model braced frame system

Floors (Fl.)	Braced Frame System			
	Displacement δ (m)		Relative Floor Displacement $\Delta\delta$ (m)	
	Ex (m)	Ey (m)	Ex (m)	Ey (m)
Fl.-20	0,046935	0,047835	0,002559	0,002616
Fl.-19	0,044376	0,045219	0,002611	0,002667
Fl.-18	0,041765	0,042552	0,002660	0,002716
Fl.-17	0,039105	0,039836	0,002714	0,002771
Fl.-16	0,036391	0,037065	0,002768	0,002825
Fl.-15	0,033623	0,034240	0,002815	0,002873
Fl.-14	0,030808	0,031367	0,002853	0,002910
Fl.-13	0,027955	0,028457	0,002876	0,002931
Fl.-12	0,025079	0,025526	0,002878	0,002934
Fl.-11	0,022201	0,022592	0,002859	0,002913
Fl.-10	0,019342	0,019679	0,002813	0,002864
Fl.-9	0,016529	0,016815	0,002734	0,002784
Fl.-8	0,013795	0,014031	0,002620	0,002667
Fl.-7	0,011175	0,011364	0,002468	0,002511
Fl.-6	0,008707	0,008853	0,002270	0,002309
Fl.-5	0,006437	0,006544	0,002024	0,002059
Fl.-4	0,004413	0,004485	0,001717	0,001745
Fl.-3	0,002696	0,002740	0,001359	0,001381
Fl.-2	0,001337	0,001359	0,000929	0,000945
Fl.-1	0,000408	0,000414	0,000408	0,000414

The graphs presented in Figure 5 and 6 were created using the table 2 and table 3 values obtained from the modeling studies. These graphs show the displacement values in the x directions for each floor of two different 20-storey reinforced concrete buildings modeled using the braced system and the shear wall frame system (Figure 5 and 6).

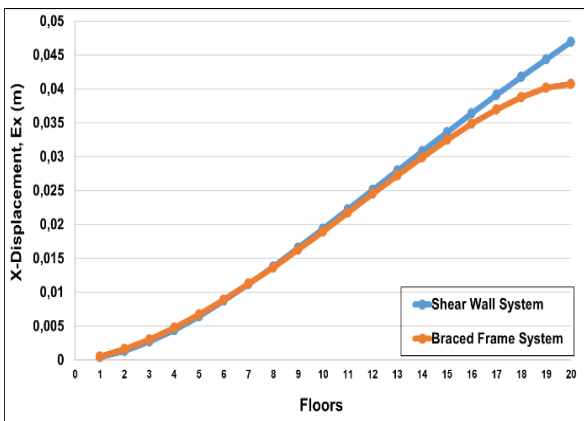


Figure 5. Graph of displacement values in x direction for each floor in 20-storey building models

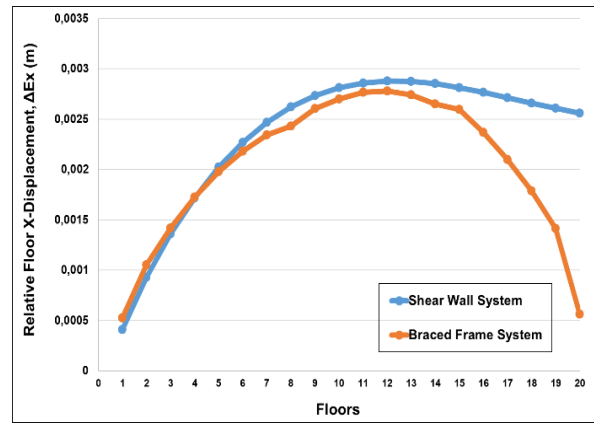


Figure 6. Graph of relative floor displacement values in x direction for each floor in 20-storey building models

Considering Figure 5 and 6, it is seen that the braced frame system performs better than the shear wall system in both graphs.

The graphs of the comparisons in the analysis of the shear wall frame system and braced frame systems for 30-storey buildings are shown in Figure 7 and 8.

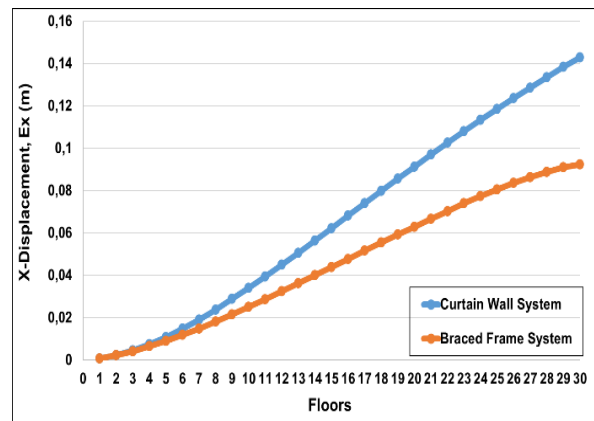


Figure 7. Graph of displacement values in x direction for each floor in 30-storey building models

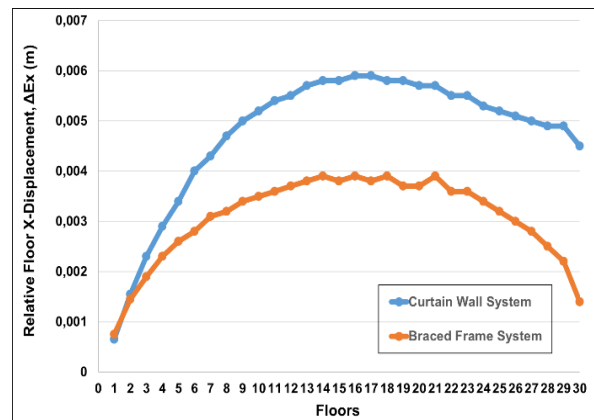


Figure 8. Graph of relative floor displacement values in x direction for each floor in 30-storey building models

A similar situation to the results obtained in 20-storey building models is also seen for 30-storey building models. As seen in both graphs, the performance of braced frame systems against seismic movements in reinforced concrete buildings is better than the shear wall frame system (Figure 7 and 8).

The graphs of the comparisons in the analysis of the shear wall frame system and braced frame systems for 30-storey buildings are shown in Figure 9 and 10.

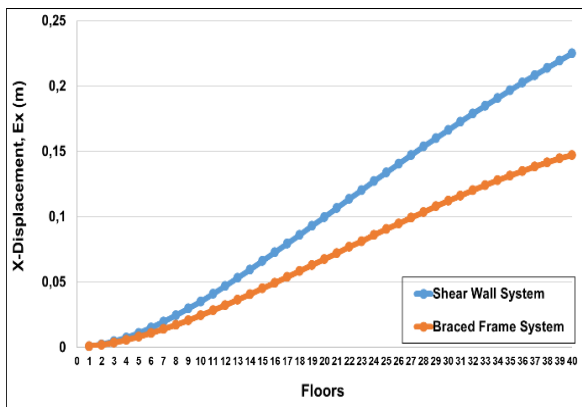


Figure 9. Graph of displacement values in x direction for each floor in 40-storey building models

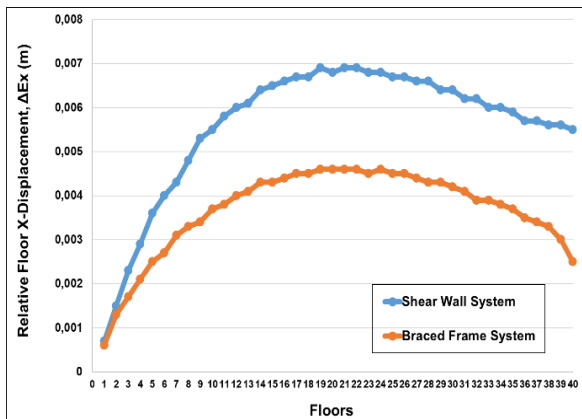


Figure 10. Graph of relative floor displacement values in x direction for each floor in 40-storey building models

It is seen that the braced frame system model performs better than the shear wall frame system model against seismic movements in 40-storey building models (Figure 9 and 10).

4. CONCLUSIONS

Improving the performance of multi-storey structures against seismic movements has been an important study topic for scientists and researchers. Especially, mitigation of the damage caused by destructive earthquakes on the structures is an issue that needs attention.

In this study, it has been indicated by modeling studies that reinforced concrete multi-storey

buildings have a better performance against seismic movements by using the braced frame system, which is generally used in steel structures.

Model studies were carried out for 20-30 and 40-storey reinforced concrete buildings. With the model outputs obtained, the displacement in the x direction cases of the braced frame system and the shear wall frame systems were examined.

As a result, it has been indicated as a result of the model studies that the braced frame system, which is not used in multi-storey reinforced concrete buildings, has a better performance against seismic movements than the shear wall frame system.

ACKNOWLEDGEMENT

This research paper prepared from the master thesis of Miraç Mesutoğlu.

REFERENCES

- AFAD, Turkey Earthquake Risk Map (2018). <https://depem.afad.gov.tr/depemtehlikehariyasi?lang=en> (Last Accessed: 20.01.2020).
- Kayvani, K. (2014). Design of High Rise Buildings: Past, Present and Future. Eds. St Smith, *23rd Australasian Conference on the Mechanics of Structures and Materials (ACMSM23)*, vol.(1) pp. 15-20. ISBN: 9780994152008.
- KeerthiGowda, B.S., Syed, T. (2014). Seismic Analysis of Multistorey Building with Floating Columns. *Proceedings of the First Annual Conference on Innovations and Developments in Civil Engineering, ACIDIC-2014*. India.
- Kovacevic, I., Dzidic, S. (2018). High-Rise Buildings: Structures and Materials. *International Burch University, Sarajevo*.
- Li, B. (2010). Enhancement of Structural Analysis of Multi-Storey Buildings by Integrating Non-structural Components into Structural System. PhD Thesis, The University of Melbourne.
- Nath, S., Debnath, N., & Choudhury, S. (2018). Methods for Improving the Seismic Performance of Structures: A Review. *In IOP Conference Series: Materials Science and Engineering* 377(1):012141.
- Phocas, M.C., & Pamboris, G. (2009). Multi-storey structures with compound seismic isolation. *Proceedings of earthquake resistant engineering structures VII*. WIT Press, Southampton, UK, 207-216.
- TBEC (2018). Turkey Building Earthquake Code, Republic of Turkey Ministry of Interior Disaster and Emergency Management Authority, Ankara, Turkey.

Turkish Standard Institute (1997). Turkish Standard, TS498: The Calculation Values of Loads used in Designing Structural Elements. Ankara, Turkey, 21 p.

Turkish Standard Institute (2007). Turkish Standard, TS-EN-1991-1-4: Actions on structures - Part 1- 4: General actions - Wind actions, Ankara, Turkey, 122 p.



© Author(s) 2021. This work is distributed under <https://creativecommons.org/licenses/by-sa/4.0/>

Thermal Anomaly Detection of Industrial Zones with MNF and ICA

Enis Arslan*¹ 

¹Cukurova University, Department of Computer Engineering, Adana, Turkey

Keywords

Land surface temperature
Thermal anomaly
Minimum noise fraction
Independent component analysis

ABSTRACT

Thermal anomalies can be detected with the help of the imagery provided by the satellite systems such as Advanced Spaceborne Thermal Emission and Reflection Radiometer (ASTER). ASTER provides five thermal bands for the effective analysis of thermal anomalies. In order to achieve this goal, considering the physical phenomena, many satellite signal processing methods and algorithms can be used. In this study, a region of steel facilities in the province of Hatay/Turkey is defined as the study area. Heat characteristics and extent of the area are represented by using four days of data from daytime and nighttime scenes. In order to define the thermal anomalies for the studied area, Land Surface Temperature (LST) was estimated by inverse Planck function approach for all TIR bands. Minimum Noise Fraction (MNF) and Independent Component Analysis (ICA) methods were applied on all thermal infrared (TIR) bands. The results of MNF and ICA components show location of the thermal anomalies for industrial complexes especially in nighttime scenes.

1. INTRODUCTION

The principal of remote sensing is to detect electromagnetic radiation emitted or reflected from the Earth in interaction with the atmosphere. TIR remote sensing techniques are commonly used in environmental studies and thermal anomaly detection (Coutts et al., 2016; Xia et al., 2018).

TIR energy emitted from vegetation, soil, water, minerals and rocks can be detected by the different regions of the electromagnetic spectrum using TIR bands. TIR sensors on a satellite system sense radiant temperature of an object that is related to its kinetic temperature. Sometimes these objects can be seen as a 'blackbody'. Blackbody is a hypothetical object which is a perfect energy absorber and emitter but at the same time which has no ability to reflect energy. It absorbs the whole spectrum regardless of the frequency. In fact, there is nothing as a blackbody but there are partial radiating objects like water, soil and rocks. By definition, emissivity is the ratio of the radiant flux emitted from an object to the value of the same object when accepted as a blackbody, which absorbs and emits all the energy at

the same temperature and wavelength. For a blackbody, emissivity is nearly 1 while for a good conductor emissivity is nearly zero. Emissivity value is affected with the wavelength, surface roughness, water vapor absorption and density of the object (Handcock et al., 2012; Islam et al., 2016). Also, it is dependent on the viewing angle of the satellite and the sensor value. Emissivity value of an object can be between 0 and 1 (Handcock et al., 2012; Moore and Paine, 2014; Ndossi and Avdan, 2016; Jensen, 2020).

In order to compensate low radiation of thermal energy emitted from the objects, satellites with high resolution sensors are designed. Aerosols like hydrometeors of cloud and water vapor negatively affect the emitted electromagnetic signals by reducing the infrared energy on the absorption bands (Moore and Paine, 2014). So, atmospheric transmissivity should be taken into consideration in the sensor design and correction of TIR images for atmospheric conditions (Handcock et al., 2012). Satellite imagery composed of thermal, near-infrared and visible bands can be used in LST estimation by using various algorithms. Split window algorithm (Wan and Dozier, 1996), single

* Corresponding Author

^{*}(enisarslan@gmail.com) ORCID ID 0000 – 0002 – 2609 – 3925

Cite this article

Arslan, E. (2020). Thermal Anomaly Detection of Industrial Zones with MNF and ICA. Turkish Journal of Geosciences, 2(1), 18-26

channel algorithm (Jiménez-Muñoz and Sobrino, 2003), inverse Planck function can be given as examples to these algorithms (Ndossi and Avdan, 2016). Radiance, Brightness temperature and Land surface emissivity are the intermediate calculation steps of the LST.

Thermal remote sensing has a variety of implementation areas such as geothermal activity (Darge et al., 2019; Gray et al., 2019; Hewson et al., 2020), coal fire research (Roy et al., 2015; Singh et al., 2020), earthquake forecasting (Ahmad et al., 2019; Wongpornchai and Suwanpravit, 2020) and heat island (Coolbaugh et al., 2007; Kuenzer et al., 2007; Wei et al., 2013; Moore and Paine, 2014; Saryshev et al., 2019). Moore and Paine (2014) studied concentrated points of heat release by using LST obtained from a different algorithm. Ndossi and Avdan (2016) studied on different algorithms to estimate LST from radiance image using ASTER data. Tiangco et al. (2008) carried out a research to derive land surface temperatures to determine the nighttime urban heat island effects. Rasul et al. (2017) reviewed researches for surface urban heat islands and surface urban cool islands.

In this study, LST was calculated by inverse Planck function as its simplicity for conversion. Minimum Noise Fraction (MNF) and Independent Component Analysis (ICA) methods were applied to TIR scenes in order to highlight thermal anomalies related with industrial factories in the study area. These methods can efficiently be used for point based thermal anomaly detection.

2. STUDY AREA and ASTER DATA

2.1. Study Area

The selected area mainly covers an industrial zone that operates on iron and steel in İskenderun city of Turkey's Hatay province. Four different areas in a square are selected in accordance with the ground truth data by using Google Earth as shown in Figure 1.

The geographic location is between with upper left latitude $36^{\circ} 46' 20''N$ and longitude $36^{\circ} 10' 27''E$, lower right latitude $36^{\circ} 39' 19''N$ and longitude $36^{\circ} 19' 43''E$.

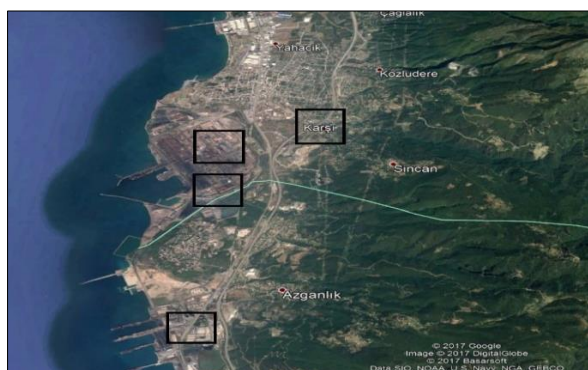


Figure 1. Google Earth image of the study area

2.2. ASTER Data

In this study, ASTER data that was obtained from Distributed Active Archive Center (DAAC) operated by U.S. Geological Survey (USGS) Earth Resources Observation and Science (EROS) Center and National Aeronautics and Space Administration (NASA) was used. ASTER is a satellite system that was launched in December 1999 as a product of NASA and Japan's Ministry of Economy developed with the aim of obtaining the land surface temperature, elevation, emissivity and reflectance data. Radiance at sensor of 15 bands is coded with digital numbers (DN). One band (Band 3B) is used for stereoscopic imagery while the other 14 bands are classified as: three bands in the visible and near infrared (VNIR), the six bands in the short wave (SWIR) and five TIR bands, with 15m, 30m and 90m spatial resolution, 8 bit (0-255), 8 bit (0-255), 12 bit (0-4095) radiometric resolution and band numbers (1-3), (4-9), (10-14), respectively. The ASTER SWIR detectors are not functioning since April 2008 and SWIR data is available before that date.

The data is highlighted with the North-up map orientation and correction by Digital Elevation Model (DEM), radiometric correction, geometric correction with GLS2000 model and cross-talk correction applied to SWIR band. The details of the data are listed in Table 1 (Meyer et al., 2015).

Table 1. The ASTER data

Date (Day, Month Year)	Time (Hour, Minute, Second)	Bands	Spatial resolution (m)
21.03.2001	08:37:47	VNIR	15
		SWIR	30
		TIR	90
13.05.2006	08:32:41	VNIR	15
		SWIR	30
		TIR	90
30.08.2005	19:35:39	SWIR	30
		TIR	90
01.01.2016	19:36:57	TIR	90

3. MATHEMATICAL MODEL of LAND SURFACE TEMPERATURE ESTIMATION

Radiance value in DN are retrieved from TIR bands of AST_L1T Advanced Spaceborne Thermal Emission and Reflection Radiometer (ASTER) data. At first, the radiance value at the sensor is calculated. After that radiance value is converted to brightness temperature and it follows the conversion from brightness temperature to LST.

3.1. Estimation of Radiance at Sensor

In the beginning, given conversion coefficients (UCC) in Table 2 (Abrams et al., 2002) for the related AST_L1T thermal bands, registered radiance values

at AST_L1T sensor in DN are converted to radiance at the sensor value in units of $W/(m^2 \cdot sr \cdot \mu m)$ by using Equation (1).

Table 2. Unit conversion coefficients (UCC)

Band Number	Unit Conversion Table	
	High gain	Normal gain
1	0.676	1.688
2	0.708	1.415
3N	0.423	0.862
3B	0.423	0.862
4	0.1087	0.2174
5	0.0348	0.0696
6	0.0313	0.0625
7	0.0299	0.0597
8	0.0209	0.0417
9	0.0159	0.0318
10		0.006822
11		0.006780
12		0.006590
13		0.005693
14		0.005225

The radiance at sensor is given as:

$$L_{\lambda} = (DN - 1) \times UCC \quad (1)$$

3.2. Brightness Temperature

Inverse Planck function is used to estimate brightness temperature as in Equation (2):

$$T_{sn} = \frac{K_2}{\ln\left(\frac{K_1}{L_{\lambda}} + 1\right)} \quad (2)$$

In this equation, T_{sn} is the brightness temperature, L_{λ} is the top of atmosphere radiance (at sensor radiance), K_1 ($Wm^2sr^{-1}\mu m^{-1}$) and K_2 ($Wm^2sr^{-1}\mu m^{-1}$) are the coefficients, in Kelvin, for ASTER data as listed in Table 3 (Abrams et al., 2002).

Table 3. K_1 , K_2 and λ coefficients for ASTER data

Band	$K_1(Wm^2sr^{-1}\mu m^{-1})$	K_2 (K)	Effective wavelength (λ) in μm
10	3047.47	1736.18	8.287
11	2480.93	1666.21	8.685
12	1930.80	1584.72	9.079
13	865.65	1349.82	10.659
14	649.60	1274.49	11.289

3.3. Land Surface Temperature Estimation

Emissivity, brightness temperature and other atmospheric values are needed to calculate LST. Planck function, split window algorithm and single channel algorithm are a few of the various algorithms that can be used to calculate LST. LST is estimated by correcting the brightness temperature with the emissivity value as shown Equation (3):

$$LST = \frac{T_{sn}}{1 + \frac{hT_{sn}}{\rho \ln \epsilon}} \quad (3)$$

In this equation, LST is the land surface temperature in K, ρ is the $h \times c/\sigma = 1.438 \times 10^{-2} mK$, λ is the effective wavelength for the related band (Table 2) and ϵ is the spectral emissivity. In this study, 0.96 value is used for ϵ where it is chosen as an average of 0.94-0.97 used for a facility in (Moore and Paine, 2014).

4. RESULTS and DISCUSSION

In the first stage of the study, LST values were computed for five TIR bands using Equation 1, 2 and 3 respectively. It is aimed to define the high LST values related with the study area in the industrial zone. The selected area mainly covers an industrial zone that operates on iron and steel. Four different areas in a square are selected in accordance with the land observation and are validated with high LST values

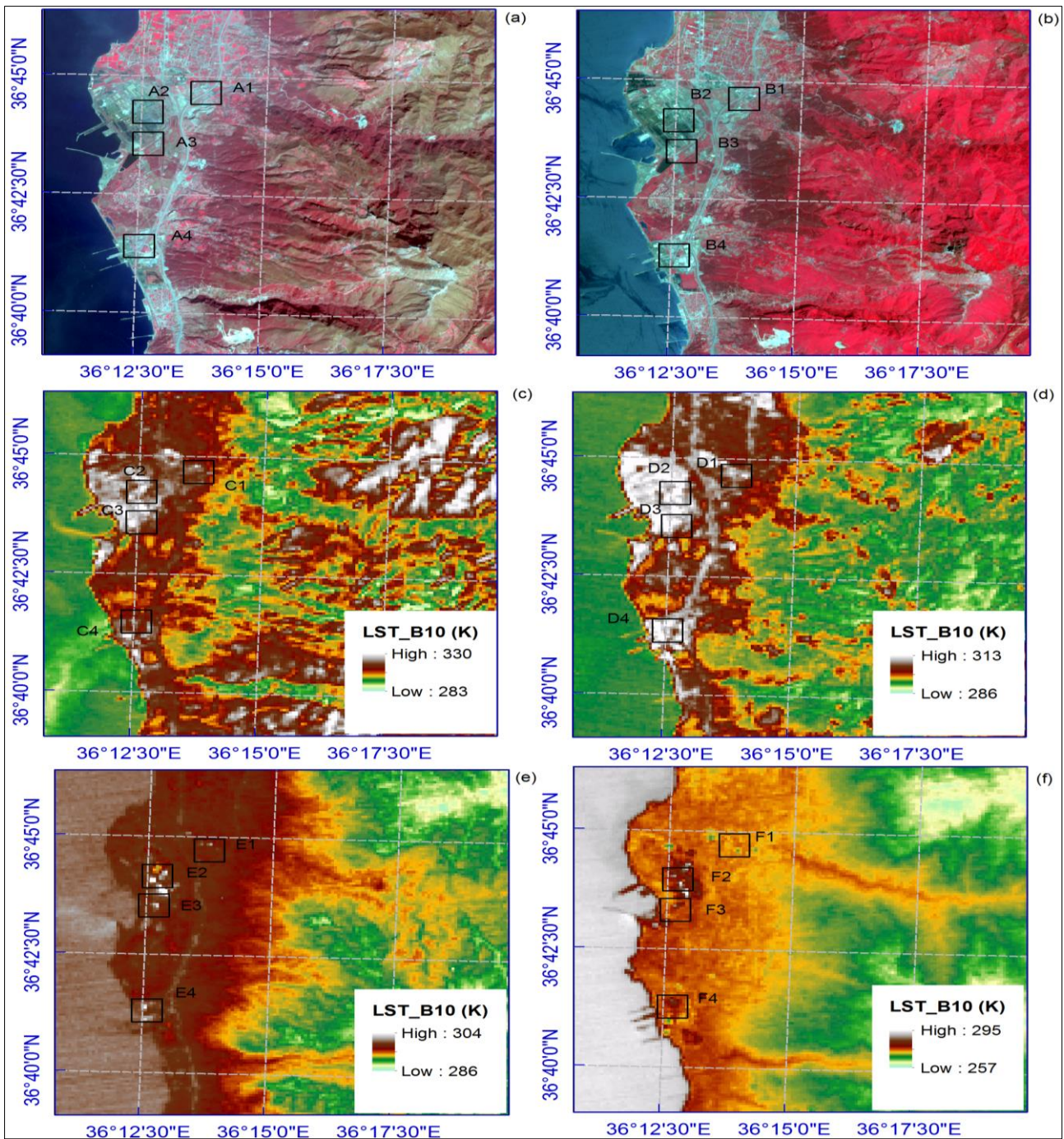


Figure 2. VNIR image of the study area (a) at 08:37:47 on 21.03.2001, (b) at 08:32:41 on 13.05.2006; LST values for TIR band10 (c) at 08:37:47 on 21.03.2001, (d) at 08:32:41 on 13.05.2006, (e) at 19:35:39 on 30.08.2005 and (f) at 19:36:57 on 01.01.2016

Figures 2a and 2b depict that, VNIR image of the study area at 08:37:47 on 21.03.2001 and at 08:32:41 on 13.05.2006, respectively. In these Figures, the high LST values are represented in squares from top to bottom as A1, A2, A3 and A4 (Figure 2a) and B1, B2, B3 and B4 (Figure 2b), respectively. In order to make comparison, two days from daytime and two days from nighttime image was selected. LST values only for band 10 is given in Figures 2c, 2d, 2e and 2f at 08:37:47 on 21.03.2001, at 08:32:41 on 13.05.2006, at 19:35:39 on 30.08.2005 and at 19:36:57 on 01.01.2016,

respectively. LST values range from 283 to 330 K (Figure 2c), 286 to 313 K (Figure 2d), 286 to 304 K (Figure 2e) and 257 to 295 K (Figure 2f).

The values in the legends for the minimum are represented in turquoise and maximum is in white colour. Out of the squared region, there are widely white coloured areas that show maximum values in daytime image as 330 K (Figure 2c; C1, C2, C3 and C4) and 313 K (Figure 2d; D1, D2, D3 and D4). The track of the road can be seen in white colour in Figure 2d and Figure 2e. It is not easy to distinguish the industrial zones in the Figures 2c and 2d. The

solar radiation coming from sun interacts with Earth and day of year affects the change of this LST values. As a result, interpretation of the daytime LST values are complex in behaviour because of this interaction.

The exact points of the thermal anomalies related with industrial zone can be seen from the nighttime image in Figure 2e (E1, E2, E3 and E4). The LST values as high as 304 K can be seen in white colour compared with the rest of the area. The similar results can be found in the other nighttime image that is given in Figure 2f (F1, F2, F3 and F4). The nighttime image more clearly depicts the areas with high thermal anomalies relative to the daytime image. Because the encircled surface has higher temperature according to the neighbouring regions at night and focused points in the scene can be easily

observed in 'white' for the industrial region with steel industry facilities.

In the second stage of the study, minimum noise fraction (MNF) analysis was applied to five thermal bands in order to determine thermal anomalies pointed out in Figures 2c, 2d, 2e and 2f. These anomalies can more clearly be determined in nighttime image as focused points (white). In order to make comparison, MNF analysis is applied to both daytime and nighttime thermal bands for the selected days. After the MNF transformation, image bands are noise reduced and decorrelated. In theory, MNF transformation is dependent on principal component analysis (PCA). In MNF, most of the information is included in the first two principal components.

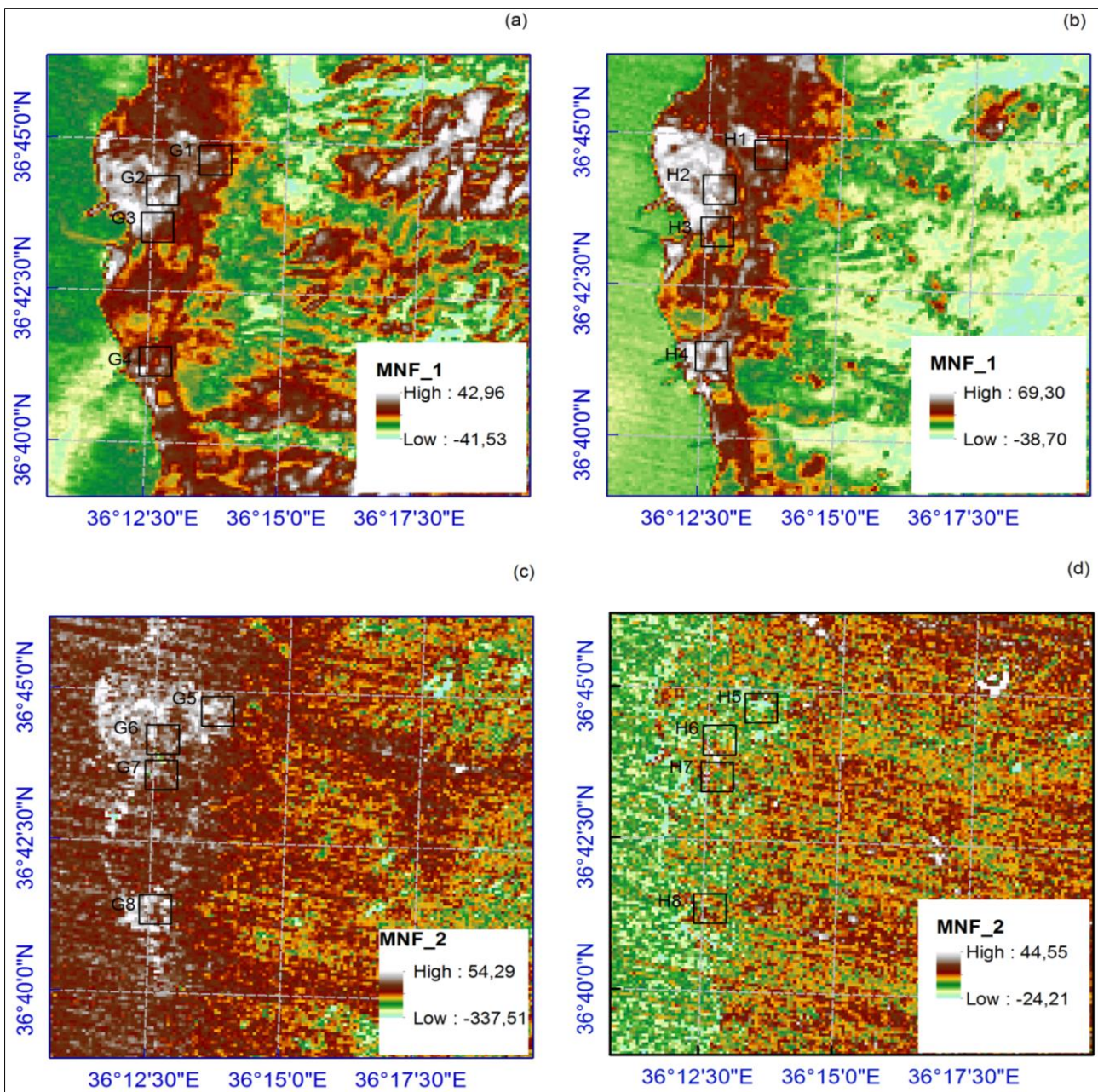


Figure 3. The first component of the MNF from the input of five thermal bands for daytime images (a) at 08:37:47 on 21.03.2001, (b) at 08:32:41 on 13.05.2006; The second component of the MNF from the input of five thermal bands for daytime images (c) at 08:37:47 on 21.03.2001, (d) at 08:32:41 on 13.05.2006

Figures 3a and 3b show the first components of the MNF transform for daytime images at 08:37:47 on 21.03.2001 and at 08:32:41 on 13.05.2006, respectively. The second components of the MNF are given at 08:37:47 on 21.03.2001 (Figures 3c) and at 08:32:41 on 13.05.2006 (Figures 3d) as well. These figures show that focused points showing steel industry facilities give high LST values because of the high temperature of furnaces. This effect represents itself as white point clusters in the images. The

squared areas highlight this clusters. There are no exact focused points in daytime images whereas it shows localized points related with thermal anomalies as white coloured pixels (G1, G2, G3, G4, H1, H2, H3 and H4). Similar results can be found for the second MNF components (G5, G6, G7, G8, H5, H6, H7 and H8). The LST daytime image includes both solar radiation effect over steel factory and furnace temperature, it is not easy separate two effects from the figures.

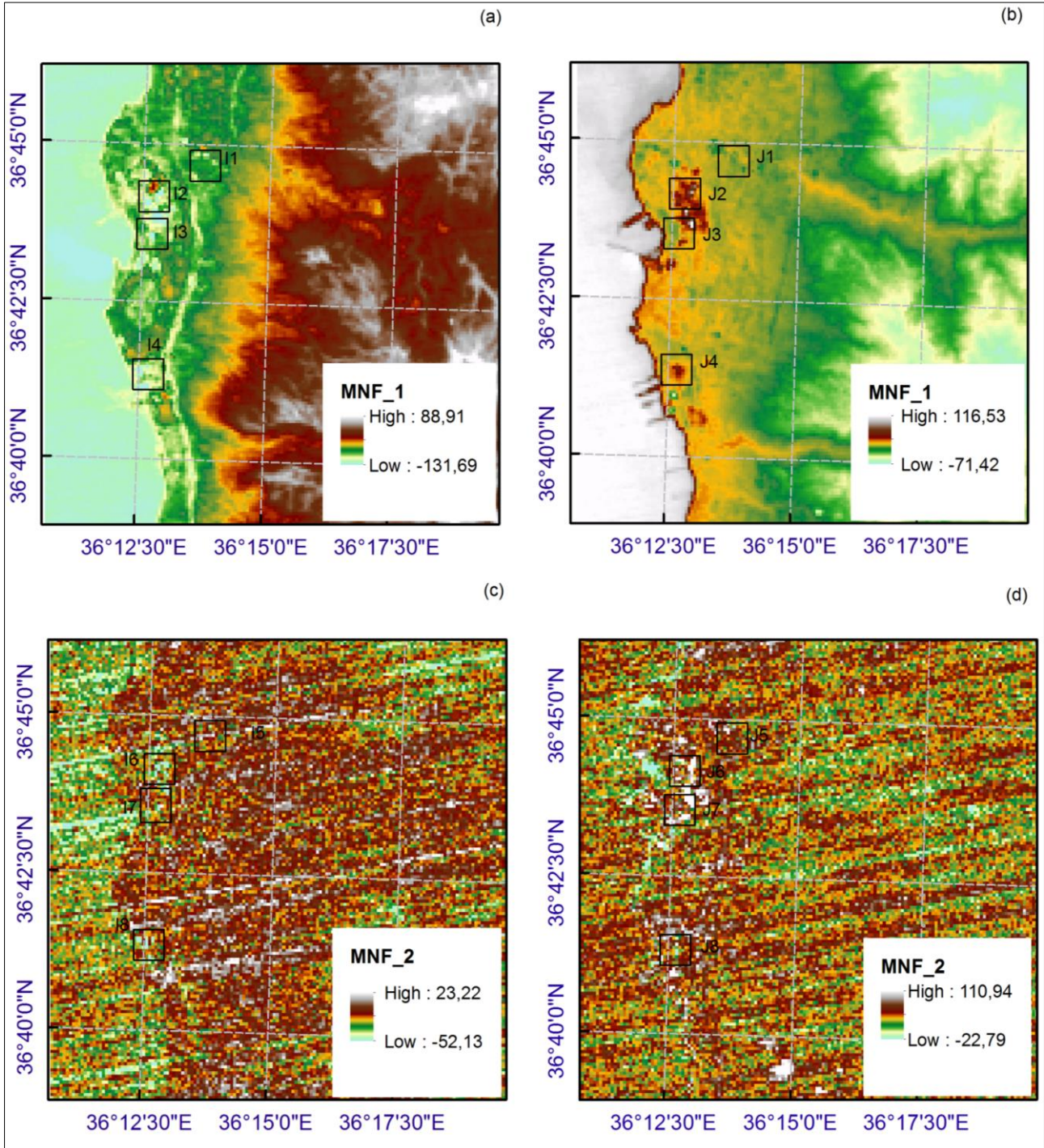


Figure 4. The first component of the MNF from the input of five thermal bands for nighttime images (a) at 19:35:39 on 30.08.2005, (b) at 19:36:57 on 01.01.2016; The second component of the MNF from the input of five thermal bands for nighttime images (c) at 19:35:39 on 30.08.2005, (d) at 19:36:57 on 01.01.2016

Figures 4a and 4b represent the first component of the MNF where Figures 4c and 4d show the second component of the MNF for nighttime images at 19:35:39 on 30.08.2005 and at 19:36:57 on 01.01.2016, respectively. Thermal anomalies can be highlighted as focused points with white colour (Figure 4a; I1, I2, I3 and I4) and brown colour (Figure 4b; J2, J3 and J4) squares. There is no distinct area that shows thermal anomalies except J6 and J7 in second component of MNF in nighttime image.

In the last stage of the study, independent component analysis (ICA) was applied to five

thermal bands in order to highlight thermal anomalies where results are represented in Figure 5. ICA analysis features the advantage of using mixed pixels when the anomalies are not evident and cannot easily be detected from the pixels. While principal component uses Gaussian statistics, ICA uses non-Gaussian statistics. ICA can be applied to multispectral remote sensing data and it can be successful even when the small part of the anomalies take place in a pixel. ICA uses mean, eigenvector, eigenvalue, principal component rotation to smooth the data.

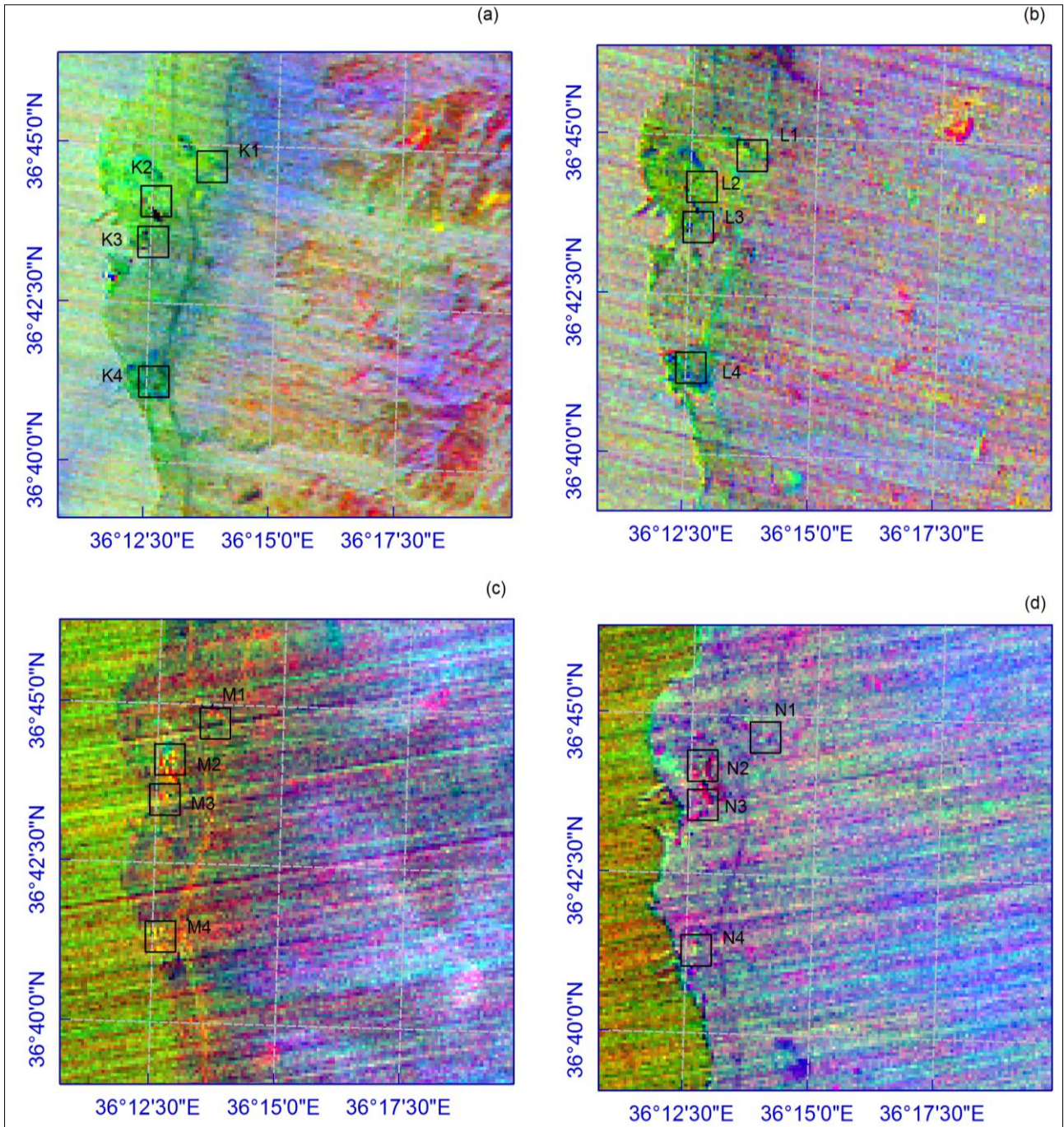


Figure 5. Red (IC3), green (IC2) and blue (IC1) band combination of the independent component analysis (ICA) of the five thermal bands (a) at 08:37:47 on 21.03.2001, (b) at 08:32:41 on 13.05.2006, (c) at 19:35:39 on 30.08.2005, (d) at 19:36:57 on 01.01.2016

Figure 5a, 5b, 5c and 5d show Red (Independent component 3-IC3), green (Independent component 2-IC2) and blue (Independent component 1-IC1) band combination of the ICA at 08:37:47 on 21.03.2001, at 08:32:41 on 13.05.2006, at 19:35:39 on 30.08.2005 and at 19:36:57 on 01.01.2016. For the daytime image in Figure 5a, black pixels in K2, K3, K4 and for the nighttime images in Figure 5c, M1, M2, M3 and M4 exactly show thermal anomalies in yellow and red coloured in a squared region. The similar results can be found in Figure 4d with N1, N2, N3 and N4 as magenta and purple coloured in a square.

5. CONCLUSION

In this study, ASTER Thermal bands was used in order to highlight thermal anomalies in an industrial zone in İskenderun city of Turkey's Hatay province where steel industry facilities are common. Furnaces operating at high temperatures emit high radiation that can be sensed as thermal anomalies in satellite imagery.

In order to detect thermal anomalies represented by focused points in the imagery, two statistical methods as MNF and ICA are used. Four different sub-regions are determined for the daytime and nighttime images for four distinct days.

At the first stage of the study, thermal anomalies in the sub-regions are verified by the calculation of LST with inverse Planck function. In the continuation of the study, MNF and ICA methods are applied to the same image data. It can be observed from the output of MNF method that the first component includes most of the information. When using this method, similar results representing the anomalies can be seen with a few exceptions. The last method, ICA, is applied to the same imagery data and 3 of the 5 bands are selected as Red (IC3) green (IC2) and blue (IC1) channels. ICA provides similar results as MNF method. Especially, nighttime imagery shows distinct colour combinations for the sub-regions highlighting the thermal anomalies.

The application of MNF and ICA methods on the ASTER image data can be helpful in point based thermal anomaly detection in a selected region and the outputs of this study gives promising results to use these methods for this purpose.

ACKNOWLEDGEMENT

The ASTER L1T data product was retrieved from the online Data Pool, courtesy of the NASA Land Processes Distributed Active Archive Center (LP DAAC), USGS/Earth Resources Observation and Science (EROS) Center, Sioux Falls, South Dakota, (https://lpdaac.usgs.gov/data_access/data_pool). This research did not receive any specific grant from funding agencies in the public, commercial, or not-for-profit sectors.

REFERENCES

- Abrams, M., Hook, S., Ramachandran, B. (2002). ASTER user handbook, version 2. *Jet propulsion laboratory, 4800*, 135.
- Ahmad, N., Barkat, A., Ali, A., Sultan, M., Rasul, K., Iqbal, Z., & Iqbal, T. (2019). Investigation of spatio-temporal satellite thermal IR anomalies associated with the Awaran earthquake (Sep 24, 2013; M 7.7), Pakistan. *Pure and Applied Geophysics*, 176(8), 3533-3544.
- Coolbaugh, M.F., Kratt, C., Fallacaro, A., Calvin, W.M., & Taranik, J.V. (2007). Detection of geothermal anomalies using advanced spaceborne thermal emission and reflection radiometer (ASTER) thermal infrared images at Bradys Hot Springs, Nevada, USA. *Remote Sensing of Environment*, 106 (3), 350-359.
- Coutts, A.M., Harris, R.J., Phan, T., Livesley, S.J., Williams, N.S., & Tapper, N.J. (2016). Thermal infrared remote sensing of urban heat: Hotspots, vegetation, and an assessment of techniques for use in urban planning. *Remote Sensing of Environment*, 186, 637-651.
- Darge, Y.M., Hailu, B.T., Muluneh, A.A., & Kidane, T. (2019). Detection of geothermal anomalies using Landsat 8 TIRS data in Tulu Moyo geothermal prospect, Main Ethiopian Rift. *International Journal of Applied Earth Observation and Geoinformation*, 74, 16-26.
- Gray, D. M., Burton-Johnson, A., & Fretwell, P.T. (2019). Evidence for a lava lake on Mt. Michael volcano, Saunders Island (South Sandwich Islands) from Landsat, Sentinel-2 and ASTER satellite imagery. *Journal of Volcanology and Geothermal Research*, 379, 60-71.
- Handcock, R.N., Torgersen, C.E., Cherkauer, K.A., Gillespie, A.R., Tockner, K., Faux, R.N. Tan, J. (2012). Thermal infrared remote sensing of water temperature in riverine landscapes. *Fluvial remote sensing for science and management*, (85) 113.
- Hewson, R., Mshiu, E., Hecker, C., van der Werff, H., van Ruitenbeek, F., Alkema, D., & van der Meer, F. (2020). The application of day and night time ASTER satellite imagery for geothermal and mineral mapping in East Africa. *International Journal of Applied Earth Observation and Geoinformation*, 85, 101991.
- Islam, T., Hulley, G.C., Malakar, N.K., Radocinski, R.G., Guillevic, P.C., & Hook, S.J. (2016). A physics-based algorithm for the simultaneous retrieval of land surface temperature and emissivity from VIIRS thermal infrared data. *IEEE Transactions*

on *Geoscience and Remote Sensing*, 55(1), 563-576.

- Jensen, J.R. (2020). *Thermal Infrared Remote Sensing Department of Geography, Lecture Notes, University of South Carolina*. Retrieved from www.gers.uprm.edu/geol6225/pdfs/06_thermal_rs.pdf
- Jiménez-Muñoz, J.C., Sobrino, J.A. (2003). A generalized single-channel method for retrieving land surface temperature from remote sensing data. *Journal of Geophysical Research: Atmospheres*, 108(D22).
- Kuenzer, C., Zhang, J., Li, J., Voigt, S., Mehl, H., & Wagner, W. (2007). Detecting unknown coal fires: synergy of automated coal fire risk area delineation and improved thermal anomaly extraction. *International Journal of Remote Sensing*, 28(20), 4561-4585.
- Meyer, D., Siemonsma, D., Brooks, B., Johnson, L., (2015). *Advanced Spaceborne Thermal Emission and Reflection Radiometer Level 1 Precision Terrain Corrected Registered At-Sensor Radiance (AST_L1T) Product, Algorithm Theoretical Basis Document* (No. 2015-1171). US Geological Survey.
- Moore, G., Paine, R. (2014). Quantifying urban-rural temperature differences for industrial complexes using thermal satellite data. *AECOM: accessed*, 15, 2018.
- Ndossi, M.I., Avdan, U. (2016). Inversion of land surface temperature (LST) using Terra ASTER data: A comparison of three algorithms. *Remote Sensing*, 2016, 8(12), 993.
- Rasul, A., Heiko, B., Claire, S., John, R., Bashir, A., José A. S., Manat, S., & Qihao, W. (2017). A Review on remote sensing of urban heat and cool islands. *Land* 6, (2) 38.
- Roy, P., Guha, A., & Kumar, K.V. (2015). An approach of surface coal fire detection from ASTER and Landsat-8 thermal data: Jharia coal field, India. *International journal of applied earth observation and geoinformation*, 39, 120-127.
- Saryschev, D.V., Kurolap, S.A., & Popova, I.V. (2019). Verification of Urban Heat Island Microclimatic Model by Using Thermal Remote Sensing Data. In *IOP Conference Series: Earth and Environmental Science* (Vol. 272, No. 2, p. 022085). IOP Publishing.
- Singh, N., Chatterjee, R. S., Kumar, D., Panigrahi, D.C., & Mujawdiya, R. (2020). Retrieval of precise land surface temperature from ASTER night-time thermal infrared data by split window algorithm for improved coal fire detection in Jharia Coalfield, India. *Geocarto International*, 1-18.
- Tiangco, M.A., Lagmay, M.F., & Argete, J. (2008). ASTER-based study of the night-time urban heat island effect in Metro Manila. *International Journal of Remote Sensing* 29, no. 10: 2799-2818.
- Xia, H., Chen, Y., & Quan, J. (2018). A simple method based on the thermal anomaly index to detect industrial heat sources. *International journal of applied earth observation and geoinformation*, 73, 627-637.
- Wan, Z., Dozier, J. (1996). A generalized split-window algorithm for retrieving land-surface temperature from space. *IEEE Transactions on geoscience and remote sensing*, 34(4), 892-905.
- Wei, C., Zhang, Y., Guo, X., Hui, S., Qin, M., & Zhang, Y. (2013). Thermal Infrared Anomalies of Several Strong Earthquakes. *The Scientific World Journal*.
- Wongpornchai, P., Suwanpravit, C. (2020). Feasibility study of thermal anomaly detection for earthquake: A case study from 2014 Mae Lao earthquake, Thailand. In *IOP Conference Series: Earth and Environmental Science* (Vol. 538, No. 1, p. 012034). IOP Publishing.



© Author(s) 2021. This work is distributed under <https://creativecommons.org/licenses/by-sa/4.0/>

Unmanned Aerial Vehicle Data Documentation of Cultural Heritage Availability: 1001 Church

Mehmet Samet Sucu*¹, Hacı Murat Yılmaz¹

¹ Aksaray University, Faculty of Engineering, Department of Geomatic Engineering, Aksaray, Turkey

Keywords

Photogrammetry Cultural
UAV
3D Model
1001 church

ABSTRACT

Photogrammetry technique is a method used for documentation of historical artifacts with measurements of archaeology for many years. Cultural heritage are common spiritual values of past and future generations. Documentation and preservation of historical monuments without damaging the natural texture are essential elements for their transfer to future generations. Cultural heritage documentation, using photogrammetric methods with the help of UAVs, increased possibilities for taking photos and therefore allows the work to be more comprehensive, reliable and realistic. This work was modeled using three different software with data from 1001 church UAVs reflecting medieval Byzantine art over Karabağ, which was considered a sacred center in the northern province of Karaman and also during the Hittites, and is thought to have been used as a Diocesan Center in ancient times. On 3D models produced using photogrammetric techniques with UAV, $m_{xy}=\pm 3.01$ cm in Agisoft Photoscan Professional software, $m_z=\pm 3.68$ cm in height error, $m_{xy}=\pm 2.26$ cm in Pix4D mapper Pro software, $m_z=\pm 1.15$ cm in height error and $m_{xy}=\pm 11.18$ cm in Visual SFM-Meshlab software, $m_z=\pm 8.11$ cm in height error. it was seen to be. Agisoft Photoscan Professional and Pix4D mapper Pro have concluded that location and height errors are acceptable in terms of Large Scale Map and Map Information Production Regulation.

1. INTRODUCTION

When it comes to cultural heritage, man-made works (paintings, sculptures), historical buildings and archaeological sites come to mind. However, the expression of cultural heritage is not limited to this; that is, it is thought to include photographs, books, documents and manuscripts. Cultural heritage is not limited to be expressed only by the concrete objects we see. There are also abstract elements that contribute to the formation of these heritages; traditions that passed from generation to generation in a society, practices and ceremonies in society. All societies contribute to world culture. For this reason, it is very important to protect all cultural heritage with laws and international agreements. Photogrammetric methods can be easily applied in cultural heritage documentation; it is seen that it is a suitable method to avoid the destruction of time, cost and historical artifacts, and that it will shed light on

this subject if it is thought that, in the following periods, relief, restitution and restoration works are considered (Uysal et al., 2013).

The techniques that are considered to be applied in the documentation of cultural heritage are based on more than one parameter; They can be classified as required precision, accuracy and time factor, object accessibility, method permits, and procurement of measuring instruments for required work (Çelik et al., 2020).

Since it uses the latest technology, it is important to use the photogrammetric method more actively in order to understand the importance of our cultural heritage and to pass it on to the generations, since it can obtain data in any format, archive it in the given digital media, and reach the result quickly with minimum error (Yakar et al., 2005).

Unmanned Aerial Vehicle (UAV); It is a kind of aircraft that does not have a pilot and passenger,

* Corresponding Author

Cite this article

*(sucumehmetsamet@gmail.com) ORCID ID 0000-0001-8225-9945
(hmuraty@gmail.com) ORCID ID 0000-0002-9725-5792

Sucu, M.S., Yılmaz, H.M. (2021). Unmanned Aerial Vehicle Data Documentation Of Cultural Heritage Availability: 1001 Churches. Turkish Journal of Geosciences, 2(1), 27-32.

carries a suitable camera and performs its duty by using smartphones and tablets as a control unit (Eroğlu, 2013).

Firstly, the researches carried out in the 1001 Church, which is the subject matter, were examined in detail. Afterwards, the necessary control points were established in the area where the 1001 Church, which is the subject of the study, was located, and the necessary control points were established, and the flight operations were carried out in the field by preparing the UAV flight plan. The field work was completed by measuring the coordinates of the control points with the help of Total station. With the data obtained, office work was initiated, the data was transferred to a UAV software, and the necessary photogrammetric operations were performed, and the three-dimensional model and documentation of the study area was made. In this way, the usability of UAV data in such applications has been examined.

In this study; The history of the Three-Dimensional Modeling and Documentation Process of UAV Data in the Documentation of Cultural Heritage has been carried out on 1001 Church, by utilizing today's advancing technology opportunities to transfer many historical and cultural heritages left to us from our past to the next generations of culture.

2. MATERIALS AND METHODS

2.1. Study Area



Figure 1. 1001 Church

Karadağ is an extinct volcanic mountain rising between the Çumra and Karaman plains and the Hotamış Swamp in the north of Karaman. Karadağ is an extinct volcanic mountain rising between the Çumra and Karaman plains and the Hotamış Swamp in the north of Karaman. There is a 1001 Church in this region which is called Değle Ören, located within the borders of Karaman Üçkuyu Village. Değle Ören,

located in Karadağ, a volcanic mountain in the north of Karaman, is approximately 35 km from the center. It is believed that 1001 church were used as the bishopric center in ancient times (Kurt, 2013). Figure 1 shows the location and view of 1001 Church in Turkey.

Among the regions listed village of Byzantine forward in terms of faith tourism in Turkey is one of the most important religious center. There are many churches and residences from the Byzantine period in the area. The churches and residences located here were established after St. Paulos, who came to Anatolia to spread Christianity, after coming to Derbe, one of the oldest settlements in Karaman. It is very important in terms of faith tourism that it is one of the places where Saint Paulos passes in Anatolia (Eyice, 1971; Kurt, 2013).

2.2. Coordinating Operations

By going to the 1001 Church located in the borders of Üçkuyu Village of Karaman Province, the area to be flight was determined. five control points and one intermediate facility, six ground control points 25 uniformly distributed locations and detail points have been established in the area to be flying, and the land direction has been completed.



Figure 2. Control points in the work area

Details were taken from the walls and side naves of the church structure to be used in aerial photographs to extract the three dimension (3D) model of the building, which is an important church structure and was used as a house and folder for a period of time.

2.2.1. Aerial imaging process

When the flight is made to the flight destination, the final checks of the UAV have been made and made ready for the flight.



Figure 3. The points where the detail is measured on the work area



Figure 4. The building control points and the distribution of control points of the side facade of the building

When the flight was finished, the UAV was lowered and the images acquired by the UAV were transferred to the computer.

2.3. Office Work

Within the scope of the study, different software studies were carried out to model cultural heritage sites in 3D with the UAV photogrammetry method. Necessary studies were carried out by using Agisoft Photoscan Professional, Pix4D mapper Pro and Visual SFM-Meshlab software.

The raw data from the total electronic distance meter were transferred to the computer. Subsequently, "x, y, z" coordinates of the detail points were calculated by using the control points with NETCAD software.

The coordinates of the points obtained were made ready for use in the software to be studied and saved in .txt format.

2.4. Creating a 3D Model with Agisoft Photoscan Professional Software

The Agisoft Photoscan Professional program was provided and the photos obtained from the field were transferred to the PC and made ready by transferring the facade and the processes were

started in Agisoft Photoscan Professional software, which is the first stage of the photogrammetric study.

While preparing the project in Agisoft Photoscan Professional:

- Entering projection values by entering raw images and GPS / IMU data of these images into the software
- Tiepoint collection process
- Entering ground control points and balancing process
- Point cloud creation process
- Mesh model creation process
- Texture dressed 3D model creation
- Provide Point cloud, 3D model and Orthophoto under the Agisoft File tab.

as the evaluation process has been completed.

Ground control points were measured with Total station and the values measured in the field were accepted as absolute values in the sensitivity survey. After this process, coordinates were obtained from the pictures produced by using UAV photogrammetric techniques.

As a result of the evaluation, images of the mesh model and orthophoto image of the old church in 1001 Church Figure 5 and 6 is also shown.



Figure 5. The texture of the resulting mesh model (texture covered)



Figure 6. As a result of the evaluation, orthophoto image of the old church in 1001 Church

2.5. 3D Model Production with Pix4D Mapper Pro Software

In this application, it has a specific workflow as in Agisoft Photoscan Professional software. We can express this order as follows.

While preparing the project in Pix4D mapper Pro:

- Opening the program and selecting the folder and giving the name
- Opening a new project
- The process of adding the pictures we take from the field
- Setting the picture coordinate system
- The process of selecting the model coordinate system
- The process of selecting the required (3D maps) data from the process options template
- The process of making the process settings
- The process of formation of the point cloud
- Adding the control points we selected
- The process of receiving reports from the system after the check points
- Obtaining orthophoto in the light of the last entered data

as the evaluation process has been completed.



Figure 7. Orthophoto and digital surface model (DEM-DSM) of the study area

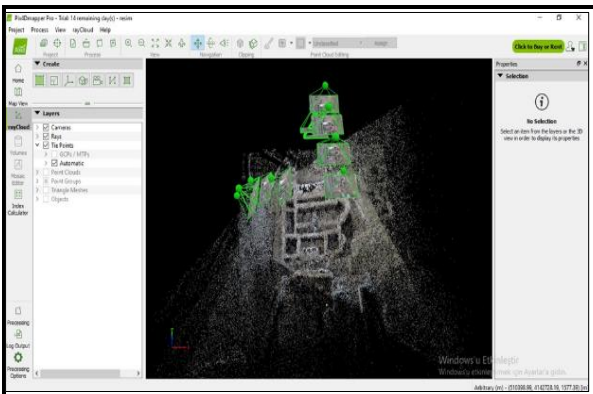


Figure 8. Orthophoto image of the workspace created with the help of Pix4D mapper Pro



Figure 9. The area where orthophoto map is created in Pix4D mapper Pro

2.6. Generating a 3D Model with Visual SFM-Meshlab Software

Visual SFM is free software and an open source software program. SFM stands for building a structural model from the image, and Visual SFM, an open source software for the production of 3D models of objects, has a general public license.

At first, the photos to be used as in Agisoft Photoscan Professional software were transferred to the software and matched with each other. This process is based on finding common details between photos using the Scale-Invariant Feature Transform combination. Then, the image-to-image mapping process automatically performs bundle balancing performed by the program, and as a result, the sparse point cloud and dense point cloud operations. Visual SFM; It also allows an open source material such as CMVS / PMVS to work integratedly. After creating a dense point cloud in Visual SFM, the model can be saved in "ply" and "nvm" formats. The recorded model has been transferred to Meshlab software, an open source software, for mesh processing and texture creation operations. By making necessary operations in the meshlab software, orthophoto image was obtained.

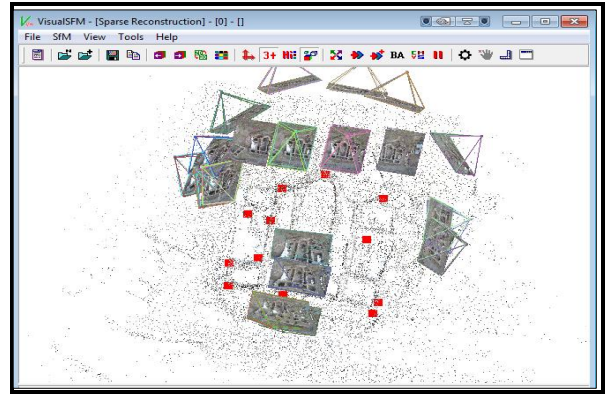


Figure 10. Point cloud that occurs after entering control points in Visual SFM software



Figure 11. Orthophoto image produced in Meshlab program

3. RESULTS

As a result of the experience obtained in the field study, the selection of UAV and digital camera is of great importance. For this reason, considering the flight sensitivity and camera resolution in our work in the 1001 Church, it was envisaged to fly with the DJI Phantom III Advanced Series and an average flight of 26 m was made. In our office, orthophoto image and DSM production processes were completed by using the package program Agisoft Photoscan Professional and Pix4D mapper Pro software, and open source software VisualSFM-Meshlab software, taking into account the drawing capabilities and other features of the software.

If we are to recover as a result of these transactions; The m_{xy} and m_z position and height errors of Agisoft Photoscan Professional and Pix4D mapper Pro software, titled "Detail Measurement Accuracy" of Large Scale Map and Map Information Production Regulation 46-1. It is seen that the detail points in the article are within the limits of location and height accuracy. This proves the accuracy of the transaction.

Using the same computer, Agisoft Photoscan Professional software completed orthophoto image and DSM production in 1 hour 55 minutes and Pix4D mapper Pro software in 24 minutes. Compared to accuracy, $m_{xy} = \pm 3.01$ cm in position error and $m_z = \pm 3.68$ cm in height error is obtained with Agisoft Photoscan Professional software, $m_{xy} = \pm 2.26$ cm in position error and $m_z = \pm 1.15$ in height error with Pix4D mapper Pro software. An accuracy of 1.15 cm was obtained. When we add Visual SFM-Meshlab software, which is an open source software in addition to both software, it was observed that there was an error of $m_{xy} = \pm 11.18$ cm in the position error obtained in our sensitivity research and $m_z = \pm 8.11$ cm in the height error.

As a result of the evaluations made according to the data obtained from these three software, Pix4D mapper Pro and Agisoft Photoscan Professional software are considered to be more suitable software than Visual SFM-Meshlab software in terms

of accuracy, time and ease of use (being a package program).

As a result; The "Detailed Measurement Accuracy" of the Large Scale Map and Map Information Production Regulation (BÖHHBÜY) in force. Using the projection coordinates and heights of the detail points, electronic tacheometry, GNSS, LIDAR or other techniques and methods; The position accuracy will be measured better than ± 7 cm (inclusive) and Helmert orthometric height accuracy will be better than ± 7 cm (inclusive)". As can be seen from here; In the light of the data we obtained from Agisoft Photoscan Professional and Pix4D mapper Pro software, it is seen that the documentation of cultural heritage using UAV and photogrammetric techniques is one that provides detail measurement accuracy. However, it is seen that the work done with Open Source Visual SFM-Meshlab software does not provide the desired accuracy according to BÖHHBÜY provisions. Documentation and three-dimensional modeling studies of historical and cultural heritage with UAV data respond to expectations using appropriate software and accuracy data can be obtained in accordance with the provisions of the regulation.

4. DISCUSSION AND CONCLUSION

In this study, the errors in the y, x and z directions obtained from Agisoft Photoscan Professional, Pix4D mapper Pro and Visual SFM-Meshlab software are given in Table 1.

Table 1. The resulting position and height errors

Software Used	m_{xy} (cm)	m_z (cm)
Agisoft Photoscan Professional	± 3.01 cm	± 3.68 cm
Pix4D mapper Pro	± 2.26 cm	± 1.15 cm
VisualSFM-Meshlab	± 11.18 cm	± 8.11 cm

When Table 1 is examined, in the sensitivity research performed on the 3D model produced by using the photogrammetric techniques with the Agisoft Photoscan Professional program, the sensitivity of the position is $m_{xy} = \pm 3.01$ cm, the height error is $m_z = \pm 3.68$ cm, and the sensitivity research done on the 3D model produced with the Pix4D mapper Pro software using photogrammetric techniques. position error $m_{xy} = \pm 2.26$ cm, height error $m_z = \pm 1.15$ cm. Finally, in the sensitivity research conducted on the model produced in Visual SFM-Meshlab software, which is open source software, the position error was found $m_{xy} = \pm 11.18$ cm, and the height error was $m_z = \pm 8.11$ cm.

According to the calculated results, it is seen that by using UAV with photogrammetric techniques,

sufficient location accuracy is provided in archaeological documentation. In this way, it can have the feature of producing litter in excavation works, modeling before and after excavation, monitoring the development of excavation phases, determining the work area and carrying the qualities that may be litter in restoration projects.

With the archaeological documentation that provides great advantage in terms of time, the desired dimensions and values can be obtained precisely on the 3D model.

When comparing our previous academic work using Agisoft Photoscan Professional;

Toprak (2014); In the study of documentation application of cultural heritage by using UAV with photogrammetric techniques; In this research, he accepted the coordinates of the location and building control points measured by the total station device as an absolute value. Coordinate differences in the y, x and z axes were taken between the coordinate values of the ground and building control points, which are accepted as the absolute value and calculated from the documentation of the cultural heritage using photogrammetric techniques, and the average position sensitivity was calculated as ± 5.01 cm by calculating the average mean errors by using these differences. seen.

In this study, it is seen that the average position sensitivity is ± 4.75 cm in our sensitivity research that we performed on the 3D model produced by using UAV with photogrammetric techniques.

As a result of the modeling we made with Pix4D mapper Pro and Agisoft Photoscan Professional programs with the same data, the following comments can be made about the results obtained when a comparison is made in terms of ease of use, time and accuracy;

Using the same computer, Agisoft Photoscan Professional software completed orthophoto image and DSM production in 1 hour 55 minutes and Pix4D mapper Pro software in 24 minutes. Compared to accuracy, position error $m_{xy} = \pm 3.01$ cm and height error $m_z = \pm 3.68$ cm are obtained in Agisoft Photoscan Professional software, while position error $m_{xy} = \pm 2.26$ cm, height error $m_z = \pm 1.15$ cm with Pix4D mapper Pro. an accuracy has been achieved.

In addition to both software, in the study made with Visual SFM-Meshlab software, an open source

software, the position error was obtained as $m_{xy} = \pm 11.18$ cm, and the height error as $m_z = \pm 8.11$ cm.

ACKNOWLEDMENT

I would like to thank Ahmet Suad TOPRAK, the staff of the Regional Development Administration of Konya Plain Project (KOP), especially for my application studies on my thesis, especially for my valuable colleague who did not withhold any support in the field.

REFERENCES

- Çelik, M. Ö., Hamal, S. N. G., & Yakar, İ. (2020). Yersel lazer tarama yönteminin kültürel mirasın dokümantasyonunda kullanımı: Alman Çeşmesi örneği. *Türkiye Lidar Dergisi*, 2(1), 15-22.
- Eroğlu, O. (2013). Flight direction based on land data in unmanned aerial vehicles Unlimited positioning system simulation study, Master Thesis, Air Force Academy Aviation and Space Technologies Institute.
- Eyice, S. (1971). Karadağ (1001 Church) and Karaman, Ist. Faculty of Letters Publications.
- Kurt, M. (2013). A study on Karadag-Mahalaç Hill (Karaman), *KMU Journal of Social and Economic Research* 15 (24): 39-45.
- Toprak, A.S. (2014). Investigation of the usability of photogrammetric techniques in unmanned aerial vehicles and engineering projects, S.Ü. Institute of Science, Konya.
- Uysal, M., Polat, N., Toprak, A. S., & Yakar, M. (2013). 3d modeling of historical doger caravansaries by digital photogrammetry.
- Yakar, M., Yıldız, F., & Yilmaz, H. M., (2005). 10. Turkey Map the documentation of Scientific and Technical Conference on the Role of historical and cultural heritage of Geodesy Photogrammetry Engineers, Chamber of Surveying Engineers.



© Author(s) 2021. This work is distributed under <https://creativecommons.org/licenses/by-sa/4.0/>

Investigation of Disasters with Different InSAR Methods

Bekir Gündoğdu*¹, Hediye Erdoğan¹, Osman Oktar¹

¹Aksaray University, Faculty of Engineering, Department of Geomatics Engineering, Aksaray, Turkey

Keywords

Disaster
SAR
InSAR
DInSAR
PS-InSAR
Change Analysis

ABSTRACT

Disasters can cause many loss of life and property every year. Although sudden disasters such as earthquakes and tsunamis cannot be detected in advance, knowing where and when disasters may occur or quickly determining the impact area of a disaster is the main factor in preventing these losses. For this reason, many different measurement methods have been developed by various professional disciplines in order to examine disasters. One of these methods is the Interferometric Synthetic Aperture Radar (InSAR) method, which is a remote sensing method. In this study, the 2015 Chile Illapel earthquake with the Differential SAR Interferometry (DInSAR) method based on the InSAR method, the vertical deformations and change analysis in the Konya Karapınar district, and the California Carr fire with the Permanent Scatterer SAR Interferometry (PS-InSAR) method were investigated. As a result of the investigations, the deformation in the LOS direction in the 2015 Chile Illapel earthquake region was found to be ~151 cm and the vertical deformations in the Konya Karapınar district were found in the range of 6.4 to -63.7 cm. Additionally, the initial and full spread area of the California Carr fire were determined.

1. INTRODUCTION

People have struggled with various disasters throughout history. Disasters can be caused by natural causes such as earthquakes, tsunamis, landslides, or due to human-induced causes such as fire, plane crash and explosions (Altun, 2018). When examined in general, it is not known where and when disasters will occur, but disasters cause similar effects in terms of their results. These are social, economic and psychological effects, especially loss of life and property. However, these factors emerge over time and can not be used to quickly determine the impact areas of disasters. Many disasters physically affect the environment where they occur. Although these effects generally occur during or immediately after the disaster, some effects may also occur before the disaster. In this way, it is possible to examine disasters. In this direction, many different measurement methods have been developed by various professional disciplines (Tomás and Li, 2017). The most effective of these methods are the remote sensing methods,

which have developed considerably in recent years. In this research, the InSAR method, which is a remote sensing method, was used.

'Radar' means range and target detection via radio waves. Radar systems have an active structure unlike optical remote sensing systems. Active systems generate their own energy. Thus, they determine the spatial and formal properties of objects on earth or in space by using the electromagnetic waves they produce. The reflection of radar signals takes place on a principle similar to that the sound wave reflects off an object and returns to the observer. The energy carried by the wave used is reflected back after reaching the object, the reflected energy is called 'echo' (Balık, 2004). Thanks to the echo, an image expressed in pixel value is produced depending on the power of the returning electromagnetic wave (Akabalı, 2002). Thus, spatial and formal features of objects on earth or in space are determined.

The first InSAR study on disasters was carried out by Massonnet and Rabaute (1993) on the California-based Landers earthquake that took

* Corresponding Author

(bekirgndgdu@gmail.com) ORCID ID 0000-0002-3913-1740
(hediye.erdogan@aksaray.edu.tr) ORCID ID 0000-0002-6470-5857
(osmanoktar@aksaray.edu.tr) ORCID ID 0000-0001-6764-0561

Cite this article

Gündoğdu, B., Erdoğan, H., Oktar, O. (2021). Investigation of Disasters with Different InSAR Methods. Turkish Journal of Geosciences, 2(1), 33-45.

place on 28.06.1992. Massonnet and Rabaute Landers used two SAR images and an existing Digital Elevation Model (DEM) 65 days before (24.04.1992) and 355 days (18.06.1993) after the earthquake to study the earthquake. As a result of the study, they determined that the 7.3 magnitude Landers earthquake caused a 112 mm movement. After these studies, the InSAR method started to be used in disaster studies. Important information was obtained about the types, characteristics and locations of disasters by using this method. 1992 Landers (Peltzer et al., 1994; Price and Sandwell, 1998), 1993 Nevada Eureka Valley (Massonnet and Feigl, 1995; Peltzer and Rosen, 1995), California Northridge (Massonnet et al., 1996; Murakami et al., 1996), 1995 Japan Kobe (Ozawa et al., 1997) earthquakes; Etna Volcano (Massonnet et al., 1995), Pu'u O'o (Rosen et al., 1996), Hawaii; Vadon and Sigmundsson, 1997), Japan Izu Peninsula (Fujiwara et al., 1998) volcanic movements; , subsidences caused by coal mining (Carnec et al., 1996; Haynes et al., 1997), subsidences in oil fields (Fielding et al., 1998) are the first examples of such studies analyzed with the InSAR method.

In this study, the 2015 Chile Illapel earthquake with the Differential SAR Interferometry (DInSAR) method based on the InSAR method, the vertical deformations and change analysis in the Konya Karapınar district with the Permanent Scatterer SAR Interferometry (PS-InSAR) method and the California Carr fire were investigated. To process the images, SARPROZ program developed by Prof. Dr. Daniele PERRISIN was used (Url-1).

2. METHOD

Since radar systems are active systems, the length of the radar antenna is directly related to the power of the transmitted wave and the capture of the reflected echo. The antenna lengths that radar systems can carry are limited. This limit is 1-2 m for airplanes and up to 10-15 m for satellites. These antenna sizes cannot physically provide sufficient resolution for distant targets. Therefore, the idea of creating a synthetic aperture was born to solve the size problems. According to this idea put forward by Carl Wiley (1951), platform motion and signal coherence are used to obtain a large antenna length. Thus, a very large antenna length would be synthesized by combining the phases of all reflections as the radar system moved between pulse transmissions. Radar systems whose antenna dimensions are synthesized in this way are called Synthetic Aperture Radar (SAR) (Elachi, 1988; Curlander and Donough, 1991). In this method, the synthetic aperture is generally created by sending a certain number of pulses in a certain time during the forward movement of the radar carried on an aircraft or a satellite (Ristau, 1999) (Figure 1).

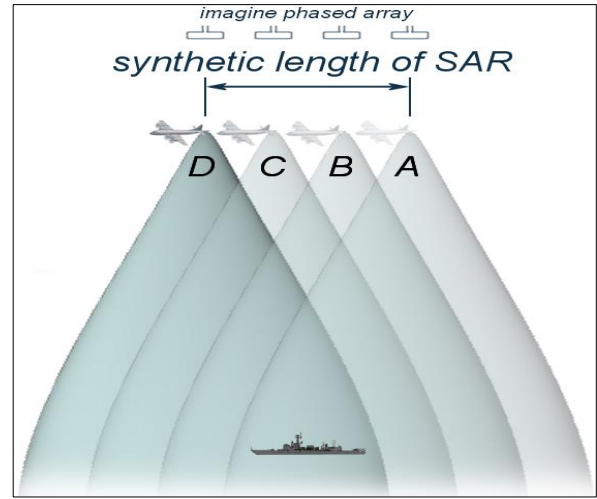


Figure 1. Working principle of synthetic aperture radars (Url-2)

Interferometry is a method of obtaining the height or height changes of a certain point by making use of the different phase and amplitude characteristics of two electromagnetic waves with the same frequency. SAR İnterferometrisi ise tek bir nokta yerine birden fazla noktanın bulunduğu SAR görüntülerinin kullanıldığı bir interferometri yöntemidir. In the InSAR method, the difference of the phase values corresponding to the point is needed to determine the height of the points on the image in the Line of Sight (LOS) direction or their movement in the LOS direction. The phase information of the SAR images is used to obtain this difference. Therefore, if there are at least two SAR images of a particular area and some of the pixels can be precisely aligned, information about the relative phase, ie height, of each point in the image can be obtained (Goldstein and Zebker 1987; Gabriel et al., 1989; Goldstein et al., 1993; Massonnet et al., 1993). In the InSAR method, SAR images are separated and matched as master image or slave image. The amplitude values of the interferogram created after the images are matched are obtained by multiplying the amplitude values of the master image with the amplitude values of the slave image. Phase values are obtained by subtracting the phase values of the slave image from the phase values of the master image. The resulting image creates an interference pattern, just like contour lines maps. The values of the pixels that make up the image range from $-\pi$ to π and each pattern transition in the image shows that there is a deformation equal to half the wavelength used in image acquisition (Figure 2) (Curlender and McDonough, 1991; Çakır, 2003; Akoğlu, 2008; Şengün, 2008; Yılmaztürk, 2015).

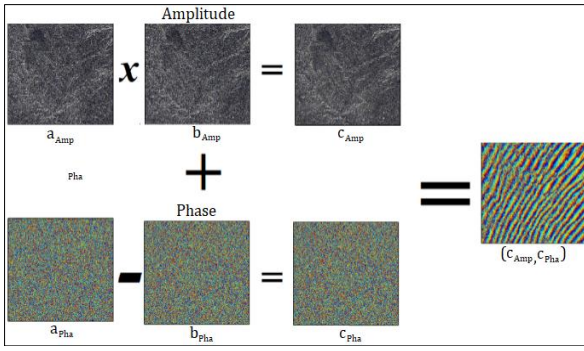


Figure 2. Interferogram formation from phase and amplitude values

DInSAR, PS-InSAR and change analysis methods used in the research are methods developed from the InSAR method. In order to use the InSAR method, at least one parameter of the SAR images that make up the interferogram must be different. This difference is called 'baseline'. (Bamler and Hartl, 1998). This difference is achieved by basically 3 different methods: single pass Along-Track method, single pass Across-Track and repeat pass method. However, although the methods differ depending on the way of image acquisition, the geometric principles of the methods are the same (Figure 3).

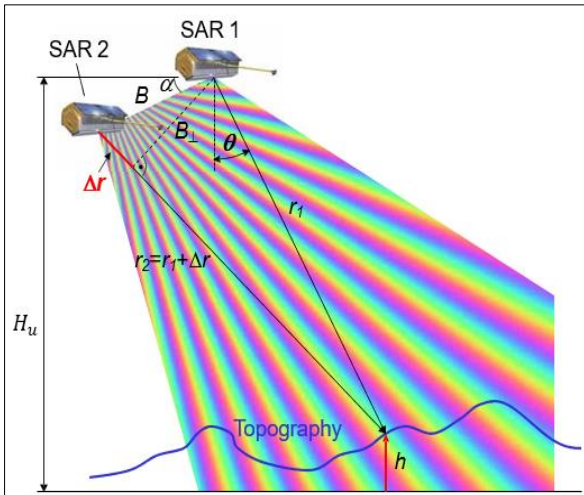


Figure 3. Interferometric SAR geometry

$$B_{\perp} = B * \sin(\theta - \alpha) \quad (1)$$

Here, the perpendicular basis is calculated by the equation in B_{\perp} 1, where α is the base slope, θ is the incidence angle, and B is the spatial basis. In order to create interferograms, the perpendicular baseline must not exceed the maximum baseline (critical baseline) (Sandwell, 2002). Phase values of an InSAR image created with two SAR images whose perpendicular baseline does not exceed the critical baseline are obtained by transferring the phase differences of the corresponding pixels of the SAR images to the image (Hanssen, 2001).

$$\phi_1 = -\frac{4\pi}{\lambda} r_1 \quad (2)$$

$$\phi_2 = -\frac{4\pi}{\lambda} r_2 = -\frac{4\pi}{\lambda} (r_1 + \Delta_r) \quad (3)$$

With Equation 2, the phase values in the first SAR image are calculated with the range of the first radar antenna (r_1). With Equation 3, the phase values in the second SAR image are calculated with the range of the second radar antenna (r_2). Here, Δ_r denotes the parallel base and is approximately equal to the difference between the two ranges.

$$\Delta\phi = \phi_1 - \phi_2 = \frac{4\pi}{\lambda} (\Delta_r) \quad (4)$$

The phase value of any pixel in the InSAR image is calculated by Equation 4, where $\Delta\phi$ is the phase difference.

$$h = H_u - r_1 \cos \theta \quad (5)$$

The height of the point from the ground (h) is calculated by Equation 5.

$$\cos(90^\circ - \alpha + \theta) = \frac{r_1^2 + B^2 - (r_1 + \Delta_r)^2}{2r_1 B} \quad (6)$$

$$\theta = \alpha - 90^\circ + \arccos\left(\frac{r_1^2 + B^2 - (r_1 + \Delta_r)^2}{2r_1 B}\right) \quad (7)$$

The angle of incidence is calculated by the cosine law, where β , α , and the distance of the radar antenna to the earth (H_u) are known and r_1 and r_2 are measured values.

2.1. DInSAR Method

Theoretically, if there is no position difference between SAR images acquired at two different times, there is no vertical base and the phase of the interferogram depends only on the deformation between acquisition times. However, when the work is put into practice, it is seen that there is a position difference between the satellite images. The undesirable phase component from this difference also includes the topography component. For this reason, DInSAR method is used to eliminate the topography component in InSAR applications. In DInSAR method, DEM is used to simulate the topographic phase. First, the DEM is converted to radar coordinates and scaled using the base line. The topographic phase obtained from the scaled DEM is subtracted from the generated interferogram and the topographic phase is eliminated (Hansen, 2001). The geometry in which the DInSAR method is used is the same as in the classical InSAR geometry (Figure 4).

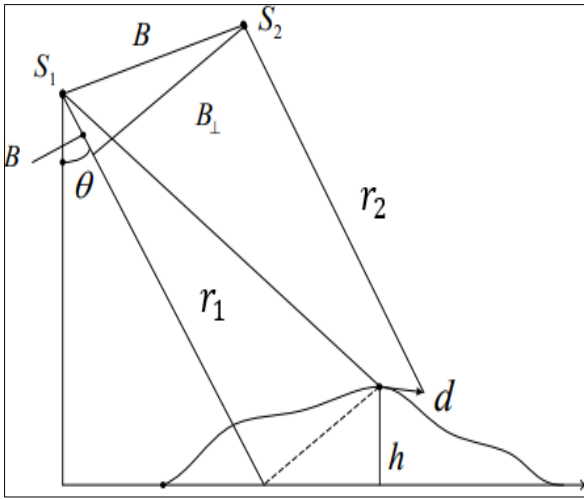


Figure 4. DInSAR geometry

Since satellites S_1 and S_2 observing the target point are in different positions, the phase component also includes the topography phase. However, since the desired phase is the differential phase, the topography phase must be eliminated.

$$\varphi_{12} = -\frac{4\pi}{\lambda}(R_1 - R_2) = \varphi_{diff} + \varphi_{top} \quad (8)$$

$$\varphi_{diff} = \varphi_{12} - \varphi_{top} \quad (9)$$

As seen in the equations 8 and 9, φ_{diff} is the differential phase and is obtained by subtracting the topography phase φ_{top} from the created interferogram.

2.2. PS-InSAR Method

The PS-InSAR technique first emerged when the Polytechnic University of Milan (POLIMI) (1999) produced and patented the PS-InSAR algorithm. In the PS-InSAR technique, it is aimed to monitor radar targets that exhibit high phase stability during the observation period. While these targets are usually objects such as buildings, metallic objects, masts, antennas found in urban areas, they can also be fixed objects such as man-made objects and rocks found in non-urban areas. The use of SAR images in the PS-InSAR method is different from the DInSAR method. As in the DInSAR method, instead of a single interferogram created from two SAR images, analysis is made over time series created with multiple interferograms (Ferretti et al., 2000). The PS-InSAR method can also be defined as the statistical analysis of the amplitudes and phases of a series of SAR images collected at different times from different angles (Figure 5).

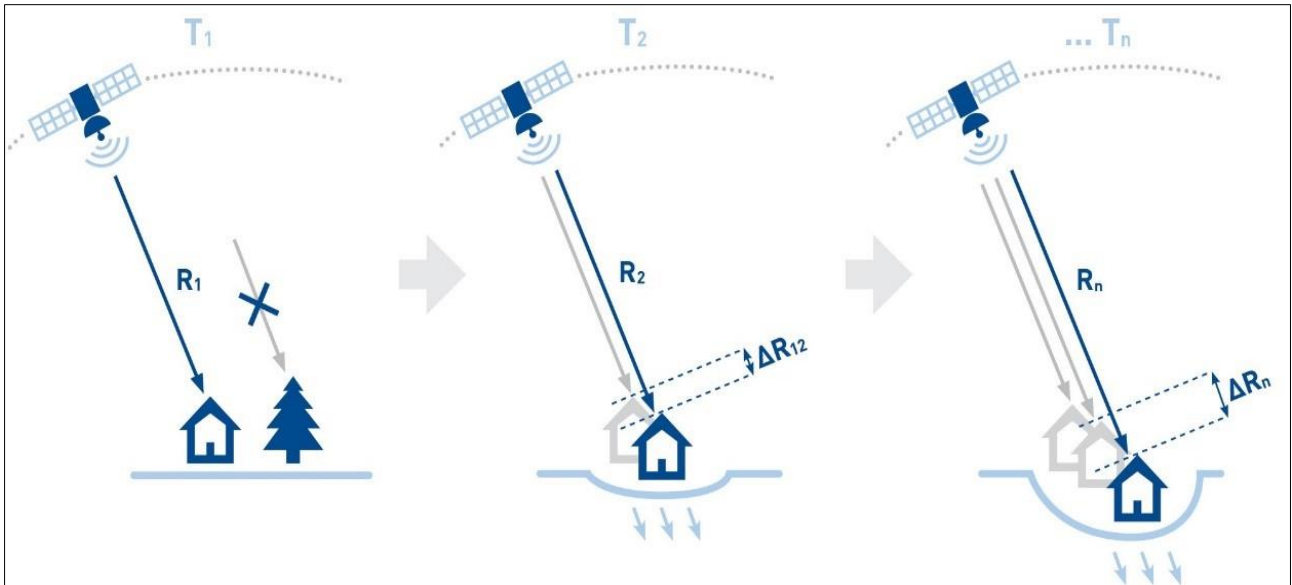


Figure 5. PS-InSAR geometry

When SAR images are acquired, the atmospheric phase has an effect that distorts the spatial correlation. However, the atmospheric phase is random and unrelated to time. The topographic phase is fixed and does not change with time. The motion-dependent phase term of the target, on the other hand, is usually time-related and may exhibit varying degrees of spatial correlation (e.g. subsidences caused from water pumping, fault displacements, locally floating areas, collapsed buildings). For this reason, phase components

coming from the atmosphere and topography can be separated according to the PS positions and the phase resulting from the movement can be left alone (Rocca et al., 2010). In the PS-InSAR method, the deformation component includes linear or non-linear phase components (Equation 10). Together with these components, the atmospheric phase component, the topographic component and the noise, the equation of a PS point is as follows (Wang et al., 2018):

$$\Delta\varphi_{diff} = \frac{4\pi}{\lambda} \Delta t \Delta v + \frac{4\pi}{\lambda} * \frac{B_{\perp}}{\rho \sin \theta} \Delta h + \Delta\varphi_{atms} + \frac{4\pi}{\lambda} \Delta D_{non-linear} + \Delta\varphi_{noise} \quad (10)$$

Given in Equation 10, Δt is the temporal basis, ρ is the slope interval, $\Delta\varphi_{diff}$ is the differential observation. The nonlinear deformation rate Δv and the residual topographic phase Δh are unknowns. In addition, if the real differential phase is greater than 2π , the phase uncertainties should also be taken into account.

$$\Delta\varphi_{x-y,ifg}^k = [a^k, b^k] * \begin{bmatrix} \Delta v_{x-y} \\ \Delta h_{x-y} \end{bmatrix} + \varepsilon (k = 1, 2, \dots, M) \quad (11)$$

Equation 11, differential observations between x and y to neighboring PS points can be expressed assuming the number of images M in a series of interferograms. The $\Delta\varphi_{x-y,ifg}^k$ component is the coefficients of the differential phase generated between x and y , a^k and b^k are mean velocity parameters and Δh_{x-y} is the residual topographic phase. Here, Δv_{x-y} and Δh_{x-y} are unknowns and must be determined using the periodogram spectral analysis method using temporal consistency maximized. Δv_{x-y} and Δh_{x-y} are converted into a frequency domain in space by periodogram spectral analysis, and analysis is made by locating single PS points with the help of temporal coherence. The remaining phase residues are due to atmospheric influences and are used to estimate the atmospheric phase scan (APS) of each interferogram. That is, the atmospheric component is estimated together with the mean velocity Δv_{x-y} and the residual topographic phase Δh_{x-y} . Atmospheric components in the differential phases can be removed by low-pass filtering in the spatial domain and by high-pass filtering in the temporal domain (Wang et al., 2018). Then, based on the PSC mesh, the positions and deformations of each point on the mesh are estimated starting from a reference point.

2.3. Change Detecting

Many different methods are used to determine the changes in the earth. Each method uses different parameters to determine the changes. Detection of changes with SAR images is usually done with the help of a pair of SAR images taken at different times in the same area. Since SAR data includes amplitude and phase information, it can be used as an indicator of change in both parameters. In the analysis of variation with amplitude values in SAR images, inconsistencies are determined by using the back-reflection properties of the signals. In the coherence mapping method, the coherence of the SAR image pair is used to determine the changes in the amplitude and phase of the pixels. Since the phases are sensitive to changes in the loop, the sensitivity of this method depends on the wavelength of the system used.

3. STUDY AREA AND MATERIALS

3.1. Chile Illapel Earthquake

Chile is a South American country occupying a long and narrow strip of land between the Andes and the Pacific Ocean. It is also part of the Pacific Ring of Fire. The Pacific Ring of Fire is highly mobile due to the collision between the Nazo and South American plates, which are highly seismic and volcanic. For this reason, earthquakes occur frequently in the region. In this study, the Chile Illapel earthquake, which took place in 2015, was investigated by DInSAR method. The 8.3 magnitude earthquake occurred off the ocean, 46 km west of Illapel. The earthquake that started at around 19.54 hours on 16.09.2015 lasted between 3 and 5 minutes. Immediately after the earthquake, three aftershocks with a magnitude of 7, 6.5 and 6.7, respectively, occurred (Figure 6).

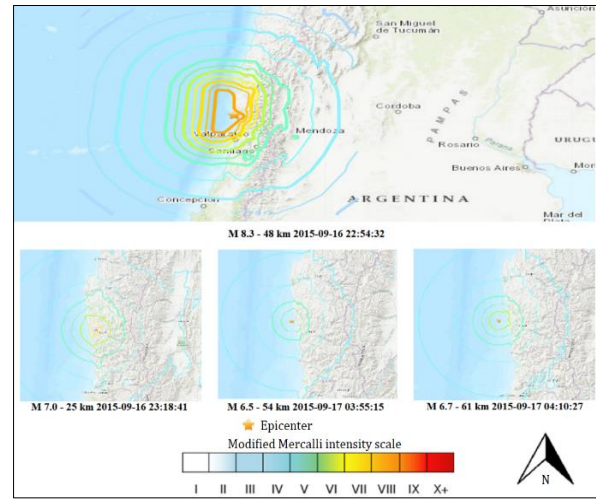


Figure 6. Impact map of the 2015 Chile Illapel and aftershocks

The impact of the earthquake covers a very large area of 93000 square kilometers. For this reason, 6 SAR images obtained from the Sentinel-1A satellite were used while examining the earthquake region.

3.2. Vertical Deformations in Konya Karapınar District

The lands of Karapınar, which is one of the most important agricultural areas and pastures in Turkey, have a calcareous structure up to 60%. For this reason, sinkhole formation is observed as a natural and dynamic process due to karstification (Orhan et al., 2020). In addition, artesian wells drilled around Karapınar cause the depletion of groundwater. For this reason, a linear deformation is observed in the region.

Within the scope of the application, 15 SAR images were selected in the 1272-day period from 02.06.2016 to 26.11.2019. Since a linear

deformation is expected while selecting the images, attention was paid to keep the time differences between consecutive images close to each other and the PS-InSAR method was used (average of 3 months).

3.3. California Carr Fire

The Carr Fire has taken its place in the literature as the 7th largest fire in California. The fire, which started on 23.07.2018 and lasted for approximately 39 days, affected a land of 229,651 decares (Figure 7).

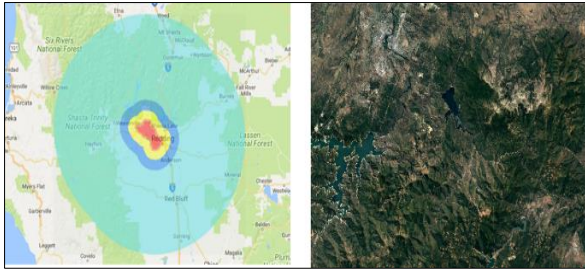


Figure 7. California Carr Fire impact zone

Since the determination of the starting point of the fire and the detection of the area of effect will be handled separately within the scope of the application, 3 SAR images were used. The fire

caused chemical deterioration due to the burning of objects in the area where it originated. Objects exposed to chemical degradation lose both their chemical and physical properties. Therefore, the phase and amplitude values of the echoes reflected from the objects before the fire and the echoes reflected after the fire are different. The soil and rocks under the forest, which are formed as a result of this difference and the burning of forests, show different reflection properties from the forests. For this reason, change analysis methods were used in the California Carr Fire application.

4. RESULTS AND DISCUSSION

4.1. Investigation of 2015 Chile Illapel Earthquake with DInSAR Method

While creating interferograms for the examination of the Chile Illapel earthquake region, 8 separate interferograms were created from 3 SAR image pairs due to the structure of the SARPROZ program. Three of the interferograms obtained via route 150 were obtained from images with frame number 700, three of them with frame number 695 and the remaining two images with frame number 690. The interferograms obtained are given in Figure 8.

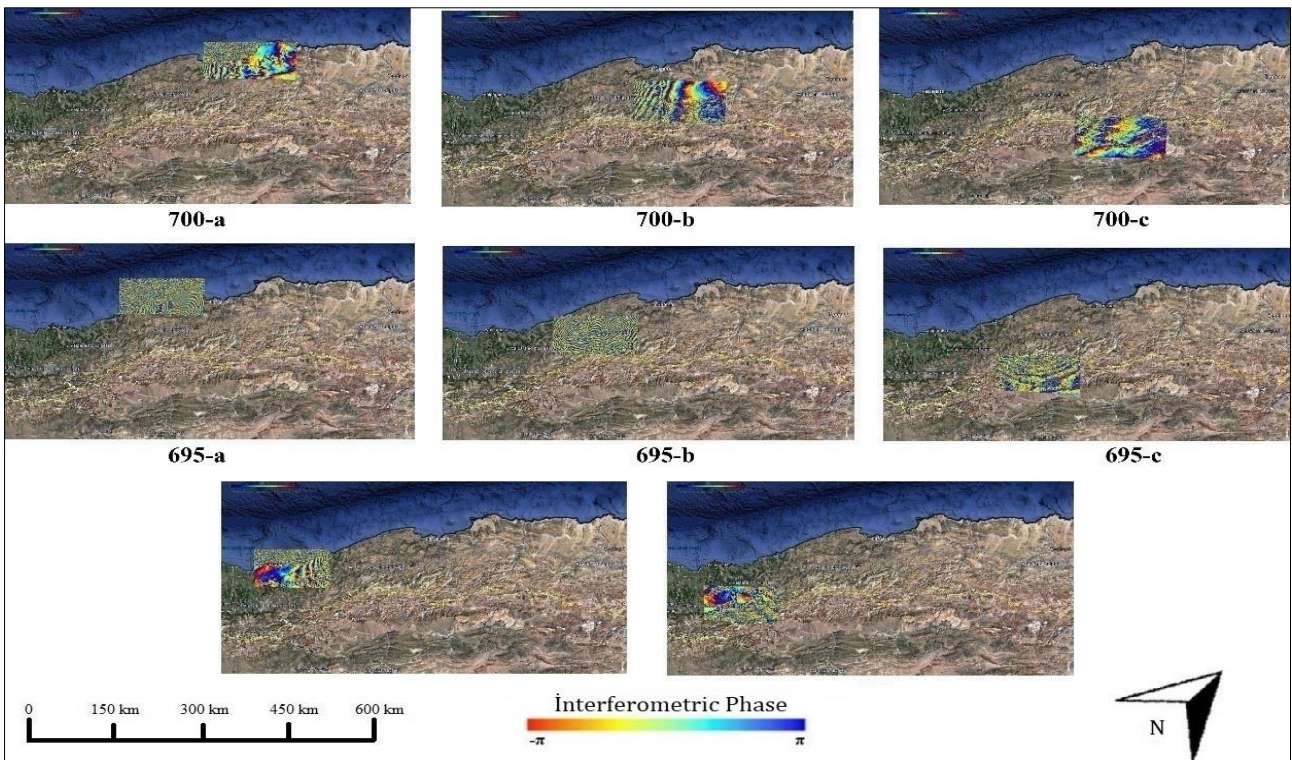


Figure 8. Interferograms generated from SAR images with track number 155

The created interferograms were combined with Google Earth and turned into a single interferogram. When the combined interferogram

was examined, 54 fringe patterns with values ranging from π to $-\pi$ were detected in the application area (Figure 9).

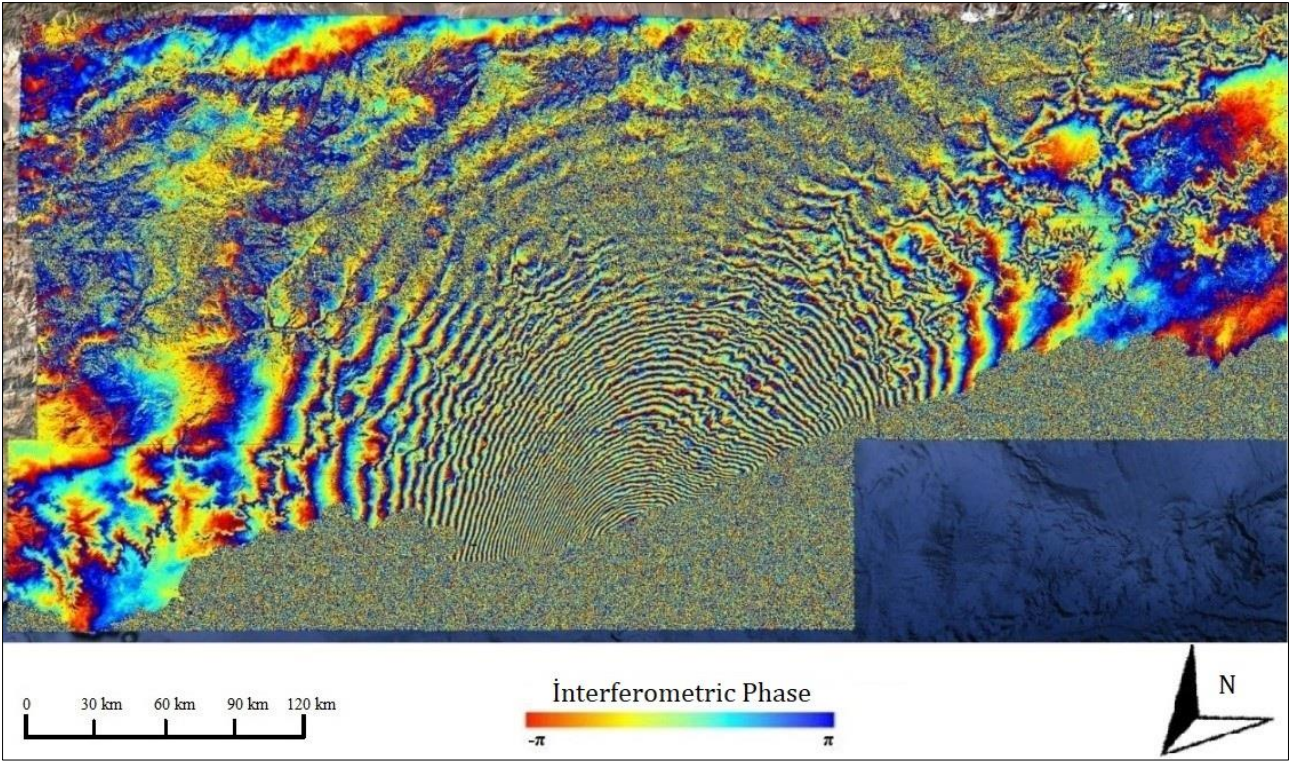


Figure 9. Combined interferogram used in the 2015 Chile Illapel earthquake application

In the DInSAR method, each pattern transition shows that there is a movement half the length of the electromagnetic wave used in image acquisition (in the LOS direction) (Curlander and McDonough, 1991; Çakır, 2003; Akoğlu, 2008; Şengün, 2008; Yılmaztürk, 2015). Since the wavelength of Sentinel-1A satellite is 5.6 cm, the deformation in the LOS direction in the 2015 Chile Illapel earthquake region was obtained as ~ 151 cm. When other studies conducted for the same region were examined, it was seen that the obtained displacement was around 150 cm (Solaro et al., 2016; Grandin et al., 2016; Klein et al., 2017).

4.2. Investigation of Vertical Deformations in Konya Karapınar District by PS-InSAR Method

In order to determine the vertical deformations in Konya Karapınar district, the application area was determined first. While determining the application area, it has been taken into consideration that the Karapınar surroundings are mostly composed of agricultural land. Therefore, the application area has been chosen to cover the center of the Karapınar district, which is a region with high reflectivity, suitable for the generation of a sufficient number of points for APS estimation and PS-InSAR method, and the surrounding rocky areas. After the images were selected, the image matching phase was started. While the images were matched, the image dated 04.06.2018 was determined as the master image and the remaining images were determined as the slave image and the matching

process was performed. Then, the APS estimation stage was passed to eliminate the atmospheric effect. In the APS estimation phase, the amplitude values such as soil and field are low, and in order to prevent the structures with disturbing factors from deteriorating the correlation, the lower limit value of agreement was determined as 0.7 based on the amplitude stability index and 719 APS points were produced (Figure 10).

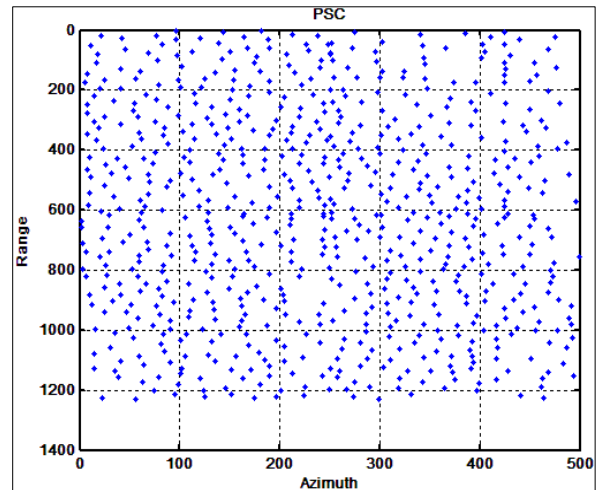


Figure 10. Points determined for APS estimation in Konya Karapınar application area

After generating the points for APS estimation and checking their consistency, the points were connected to each other using the Delaunay triangulation method and a network of 2136 triangles was obtained (Figure 11).

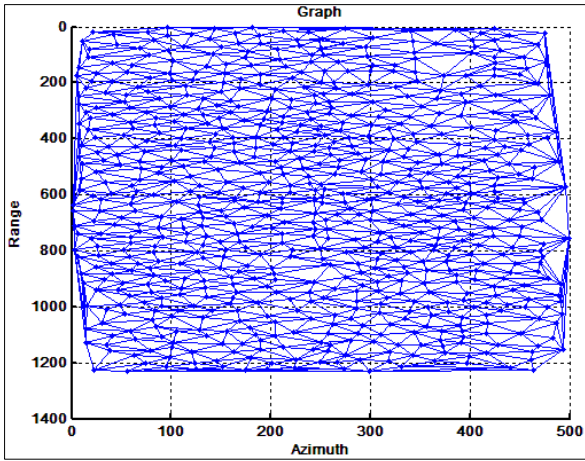


Figure 11. Delaunay triangle network formed with APS points determined in Konya Karapınar application area

Afterwards, atmospheric phase estimation was made and the atmospheric effect was eliminated. After the atmospheric effect was removed, the process of determining the PS points was started. While selecting the PS points, the lower limit of the agreement value was selected as 0.65 based on the amplitude stability index and 9478 points were determined (Figure 12).

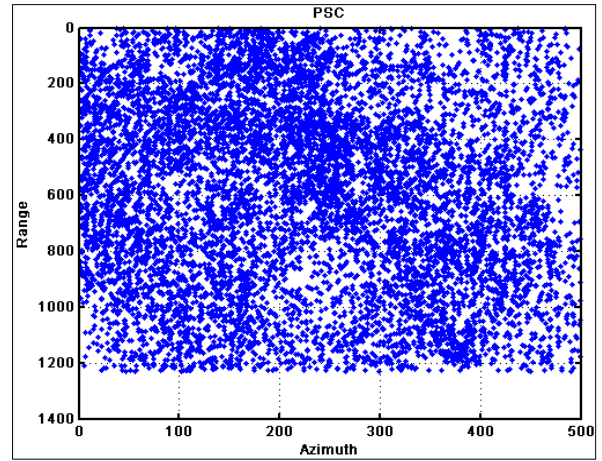


Figure 12. PS points determined in Konya Karapınar application area

The determined points were filtered by choosing a temporal consistency value of 0.8 and reduced to 5713 points. Filtered points were opened on Google Earth using time series of the 5713 points. When the annual average movements of the obtained PS points in the LOS direction are examined, it has been determined that the movements of the points in the district center vary between -5 mm and -10 mm, the movements of the points in the region between the district center and the agricultural lands vary between -10 mm and -20 mm, and the movements of the points near the agricultural areas vary between -20 mm and -50 mm (Figure 13).

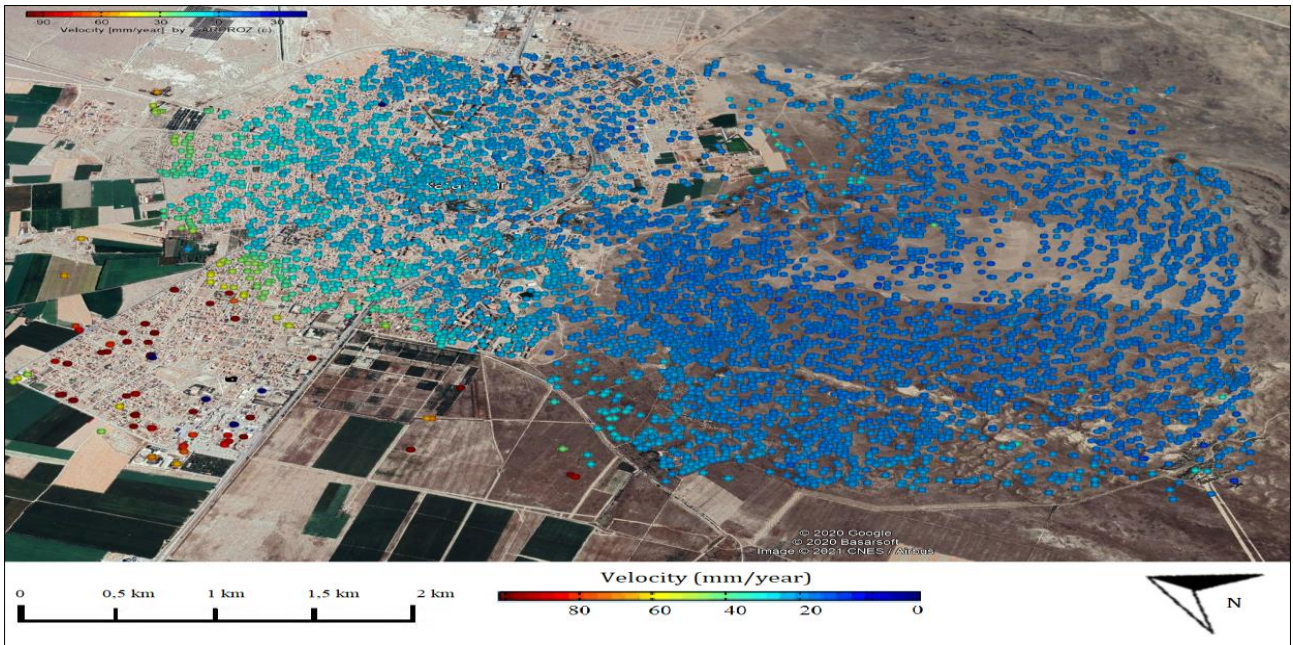


Figure 13. Distribution of PS points with a temporal correlation of 0.7 and above determined in Konya Karapınar application area

However, the deformation in the application area occurs vertically in terms of the reasons for its occurrence. For this reason, deformation values in

the LOS direction were converted to vertical deformation values (Table 1)

Table 1. The average values of the annual average movements in the LOS direction and their vertical equivalents of the PS points used in Konya Karapınar application, according to the distribution of the points

Area	LOS (mm)	Vertical (mm)
Center of district	[-5,-10]	[-6,4, -12,7]
The area between the center of district and agricultural lands.	[-10,-20]	[-12,7, -25,5]
Areas close to agricultural fields	[-20,-50]	[-25,5, -63,7]

4.3. Investigation of California Carr Fire with Change Analysis

Since the determination of the starting point of the fire and the detection of the area of effect will be handled separately within the scope of the application, 3 SAR images were used. After the images were selected, the matching phase of the images was started. While matching the images, the image dated 12.07.2018 to be used in both applications was determined as the master image, and the images dated 24.07.2018 and 10.09.2018 were determined as the slave image. After the images were matched, the application phase was started. In both applications, the change detection was made with the method in which only amplitude values were used and the general coherent map using phase and amplitude values.

In the images created with the SARPROZ program with the first method in which only the amplitude values of the images are used, the places where the amplitude values of the pixels in the master image are less than the amplitude values of the pixels in the slave image are expressed with yellow pixels, and the places where they are more are expressed with blue pixels. In this way, the starting point of the fire and the effect area of the fire were determined by determining the increasing amplitude values (blue colored pixels) due to the emergence of the rock and soil under the forest lands destroyed by the fire. In the second method, in which both amplitude and phase values are used,

the regions under the effect of shadowing or the places where the harmony decreases in the general coherent maps created by the SARPROZ program are expressed with black toned pixels. In this way, the starting point of the fire and the effect area of the fire were determined by determining the places where the consistency fell. In the study, in which the starting point of the fire was determined, the change analysis using the amplitude values was performed, the lower limit value of the change was determined as 0.14, and the differences below this value were filtered by assuming noise. The filter window size was determined as 25 in order to reduce the estimation uncertainty and increase the consistency without reducing the spatial resolution too much, since the application area consists of dense forest land. After determining the noise threshold and filter window size, an image was created by taking the difference of the amplitude values of the corresponding pixels of the SAR images dated 12.07.2018 and 24.07.2018. After the image was created, the blue pixels were determined and the area where the fire started was determined. In the second method, in which phase and amplitude values are used, a general coherent map was created using images dated 12.07.2018 and 24.07.2018. In the map created, the areas where the adaption decreased were determined by black toned pixels and the area where the fire started was determined. Then, the two images were combined on Google Earth to better observe the starting point of the fire (Figure 14).

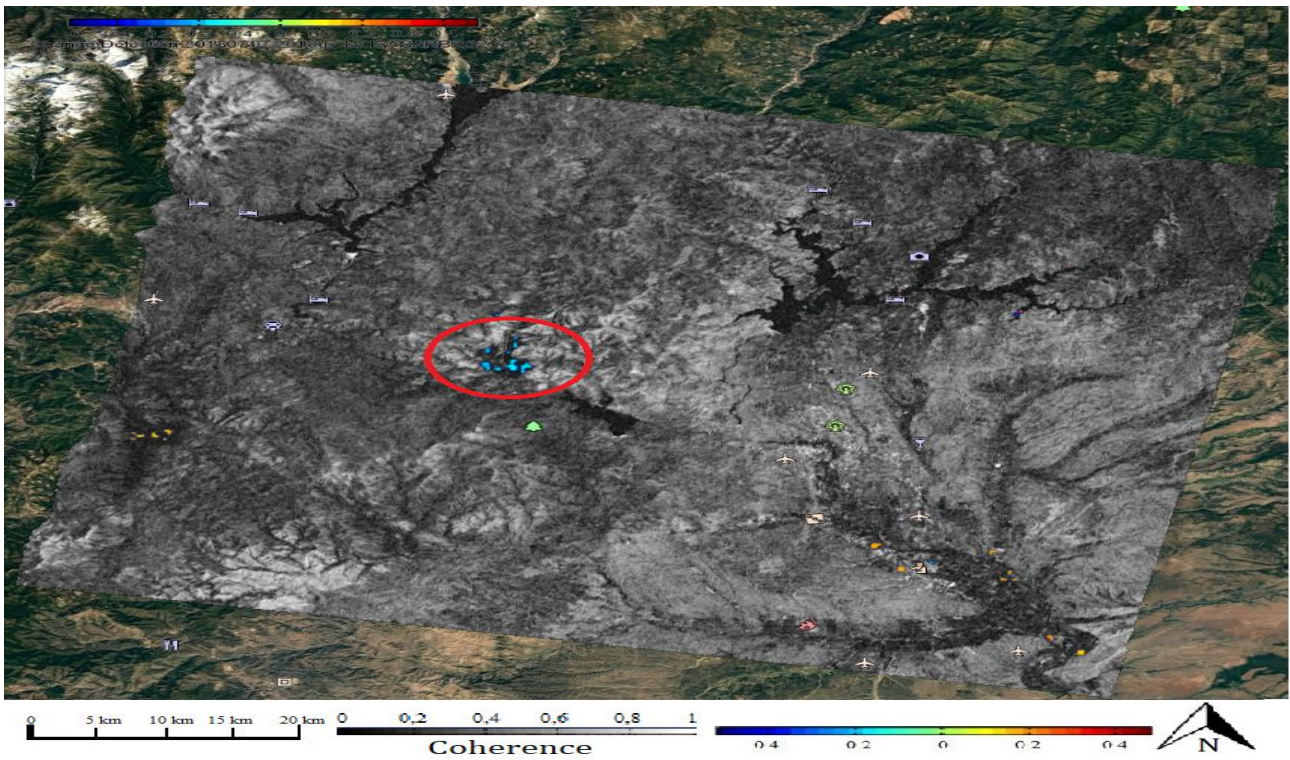


Figure 14. The starting point of the California Carr Fire, which was determined as a result of combining the images from the two methods

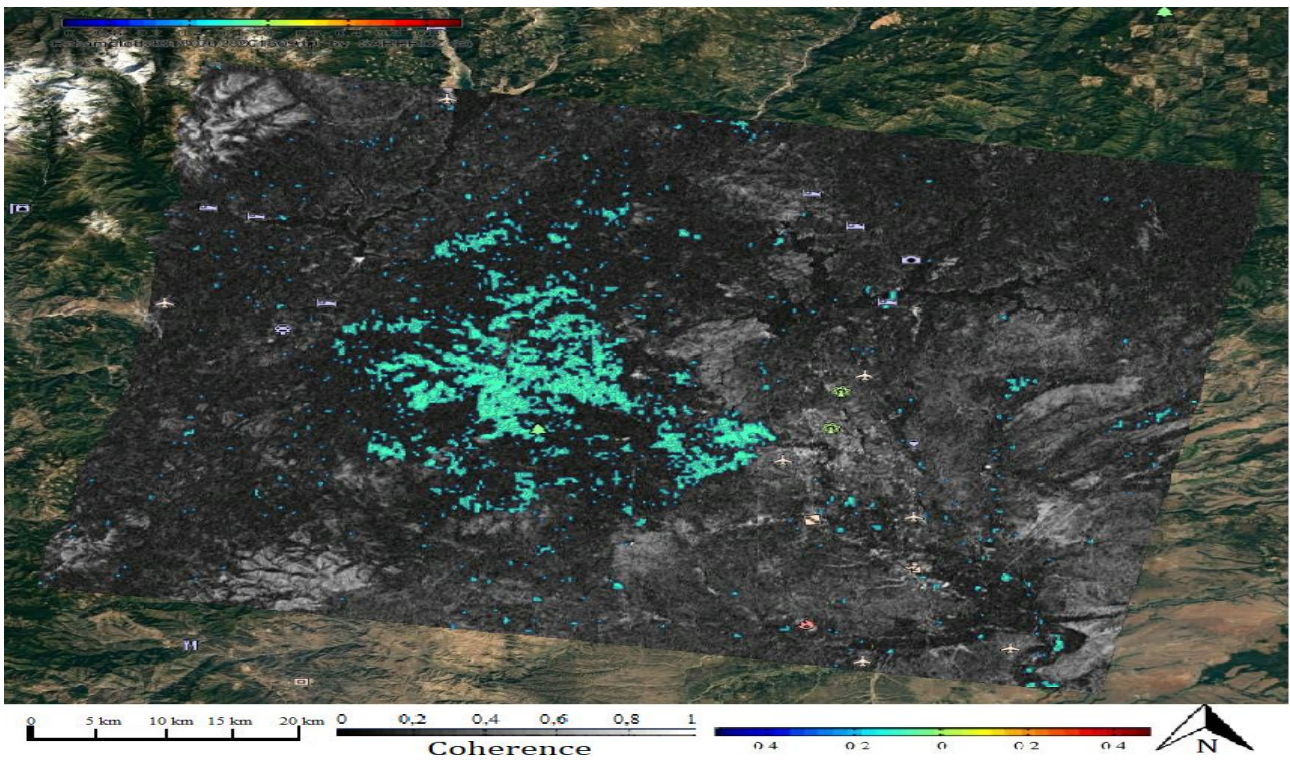


Figure 15. The effect area of the California Carr Fire which is determined as a result of combining the images from the two methods

In the analysis in which the effect area of the California Carr Fire was determined, firstly, the change analysis method with the amplitude values of SAR images was used. As a result of the applications made with different values, it was seen

that the best results were obtained when the lower limit value was determined as 0.142. The filter window size remained the same as the value in the application where the starting point of the fire was determined. After determining the noise threshold

and filter window size, an image was created by taking the difference of the amplitude values of the corresponding pixels using the SAR images dated 12.07.2018 and 10.09.2018. The area where the fire started was determined by determining the blue pixels in the image created after the image was created. In the second method, in which phase and amplitude values are used, a general coherent map was created using images dated 12.07.2018 and 10.09.2018. Areas of influence of the fire were determined by determining the black toned pixels where the coherent decreased in the map created. Then, the two images were combined on Google Earth in order to better observe the impact area of the fire (Figure 15).

5. CONCLUSION

The research examining the 2015 Chile Illapel earthquake reveals the ability of the InSAR method to map large areas such as 93000 square kilometers, which is the entire application area of the 2015 Chile Illapel earthquake. The research examining the Vertical Deformations in Konya Karapınar shows that linear deformations can be determined from the measurements made with the PS-InSAR method and the average velocities of the deformations can be calculated. In addition, it has been observed that the LOS directional deformations obtained as output can be converted to real deformation values with a simple transformation if the deformation is unidirectional. In this context, unidirectional deformations such as collapse, abrasion, and sinkhole formations can be determined by the PS-InSAR method. Research examining the California Carr Fire shows that fire detection studies with Change detection are successful and can be used in the detection of fire areas.

When the whole research is considered completely, it is seen that the InSAR method can be used in different disaster researches. In addition, Sentinel-1 satellite images, which are free of charge, with a wavelength of 5.6 cm (C-band) and a period of 12 days facilitate research on disasters such as earthquakes, tsunamis, fires, and explosions in any region. Since the satellite system can take images in a fixed period and has been active since 2014, it enables the investigation of disasters such as volcanic movements and landslides with time series.

ACKNOWLEDGEMENT

This article was produced from Bekir GÜNDOĞDU's master thesis. The Scientific and Technological Research Council of Turkey (TÜBİTAK) provided financial support to Bekir GÜNDOĞDU's graduate education within the scope of the 2210/A General Domestic Post Graduate Scholarship Program. The authors thank Prof. Dr. Daniele PERRISIN for giving permission free access to the SARPROZ software.

REFERENCES

- Akabalı, A. (2002). Stereo yapay açıklıklı radar görüntülerinden otomatik sayısal yükseklik modeli üretilmesi ve doğruluğunun araştırılması (MSc thesis) Yıldız Technical University, Istanbul, Turkey.
- Akoğlu, A. M. (2008). Analysis and modelling of the earthquake surface deformation with SAR interferometry: Case studies from Turkey and the world (PhD thesis) Istanbul Technical University, Istanbul, Turkey.
- Altun, F. (2018). Afetlerin ekonomik ve sosyal etkileri: Türkiye örneği üzerinden bir değerlendirme. *Sosyal Çalışma Dergisi*, 2(1), 1-15.
- Balık Şanlı, F. (2004). Elektro-optik ve SAR uydu görüntüleri ile arazi bitki örtüsünün belirlenmesi (PhD thesis) Yıldız Technical University, Istanbul, Turkey.
- Bamler, R., & Hartl, P. (1998). Synthetic aperture radar interferometry. *Inverse Problems*, 14(4), 1-54.
- Carnec, C., Massonnet, D., & King, C. (1996). Two examples of the use of SAR interferometry on displacement fields of small spatial extent. *Geophysical Research Letters*, 23(24), 3579-3582.
- Curlander, J.C., & McDonough, R.N. (1991). Synthetic aperture radar systems and signal processing. John Wiley & Sons, Inc., Press, New York, USA.
- Çakır, Z. (2003). Analysis of the crustal deformation caused by the 1999 İzmit and Düzce Earthquakes using synthetic aperture radar interferometry (PhD thesis). Istanbul Technical University, Istanbul, Turkey.
- Elachi, C. (1988). Spaceborne radar remote sensing: Applications and techniques. *IEEE Press*, New York, ABD.
- Ferretti, A., Prati, C., & Rocca, F. (1999). Process for radar measurements of the movement of city areas and landsliding zones. EPO Patent NO: EP1183551B, European Patent Office.
- Ferretti, A., Prati, C., & Rocca, F. (2000). Nonlinear subsidence rate estimation using permanent scatterers in differential SAR interferometry. *IEEE TGRS*, 38, 5, 2202-2212.
- Fielding, E.J., Blom, R.G. & Goldstein, R.M. (1998). Rapid subsidence over oil fields measured by SAR interferometry. *Geophysical Research Letters*, 25(17), 3215-3218.

- Fujiwara, S., Rosen, P.A., Tobita, M., & Murakami, M. (1998). Crustal deformation measurements using repeat-pass JERS 1 synthetic aperture radar interferometry near the Izu Peninsula, Japan. *Journal of Geophysical Research: Solid Earth*, 103(B2), 2411-2426.
- Gabriel, A.K., Goldstein, R.M., & Zebker, H. (1989). Mapping small elevation changes over large areas: Differential radar interferometry. *Journal of Geophysical Research*, 94, 9183-9191.
- Goldstein, R.M., & Zebker, H.A. (1987). Interferometric radar measurement of ocean surface currents. *Nature*, 328(6132), 707-709.
- Goldstein, R.M., Engelhardt, H., Kamb, B., & Frolich, R. M. (1993). Satellite radar interferometry for monitoring ice sheet motion: Application to an Antarctic ice stream. *Science*, 262(5139), 1525-1530.
- Graham, L.C. (1974). Synthetic interferometer radar for topographic mapping. *Proceedings of the IEEE*, 62(6), 763.
- Grandin, R., Klein, E., Métois, M., & Vigny, C. (2016). Three-dimensional displacement field of the 2015 Mw8.3 Illapel earthquake (Chile) from across-and along-track Sentinel-1 TOPS interferometry. *Geophys. Res. Lett.*, 43(6), 2552-2561.
- Hanssen, R.F. (2001). Radar interferometry data interpretation and error analysis. Kluwer Academic Publishers, Dordrecht, Hollanda.
- Haynes, M., Capes, R., Lawrences, G., Smith, A., Shilston, D., & Nicholls, G. (1997). Major urban subsidence mapped by differential SAR interferometry, *The 3rd ERS Symposium (ESA)*. Florence, Italy, 18-21.
- Massonnet, D., Briole, P., & Arnaud, A. (1995). Deflation of Mount Etna monitored by spaceborne radar interferometry. *Nature*, 375(6532), 567-570.
- Massonnet, D., & Feigl, K. L. (1995). Discrimination of geophysical phenomena in satellite radar interferograms. *Geophysical Research Letters*, 221(2), 1537-1540.
- Massonnet, D., Rossi, M., Carmona, C., Adragna, F., Peltzer, G., Feigl, K., & Rabaute, T. (1993). The displacement field of the Landers earthquake mapped by radar interferometry. *Nature*, 364(6433), 138-142.
- Meyer, B., Armijo, R., Massonnet, D., De Chabaliér, J. B., Delacourt, C., Ruegg, J.C., & Papanastassiou, D. (1996). The 1995 Grevena (northern Greece) earthquake: Fault model constrained with tectonic observations and SAR interferometry. *Geophysical Research Letters*, 23(19), 2677-2680.
- Murakami, M., Tobita, M., Fujiwara, S., Saito, T., & Masaharu, H. (1996). Coseismic crustal deformations of 1994 Northridge, California, earthquake detected by interferometric JERS 1 synthetic aperture radar. *Journal of Geophysical Research: Solid Earth*, 101(B4), 8605-8614.
- Orhan, O., Kırtılođlu, O.S., & Yakar, M. (2020). Konya kapalı havzası obruk envanter bilgi sisteminin oluşturulması. *Geomatik*, 5(2), 81-90.
- Ozawa, S., Murakami, M., Fujiwara, S., & Tobita, M. (1997). Synthetic aperture radar interferogram of the 1995 Kobe Earthquake and its geodetic inversion. *Geophysical Research Letters*, 24(18), 2327-2330.
- Peltzer, G., Hudnut, K. W., & Feigl, K. L. (1994). Analysis of coseismic surface displacement gradients using radar interferometry: New insights into the Landers earthquake. *Journal of Geophysical Research: Solid Earth*, 99(B11), 21971-21981.
- Peltzer, G., & Rosen, P. (1995). Surface displacement of the 17 May 1993 Eureka Valley, California, earthquake observed by SAR interferometry. *Science*, 268(5215), 1333-1336.
- Price, E.J., & Sandwell, D.T. (1998). Small-scale deformations associated with the 1992 Landers, California, earthquake mapped by synthetic aperture radar interferometry phase gradients. *Journal of Geophysical Research: Solid Earth*, 103(B11), 27001-27016.
- Ristau, J.P. (1999). Applications of synthetic aperture radar interferometry in the study of the nahanni earthquake region (MSc thesis) Manitoba University, Manitoba, Canada.
- Rocca, F., Prati, C., & Ferretti, A. (2010). Space-borne SARs: impact of wavelengths and scan modes on ground motion studies. *Annals of GIS*, 16(2), 69-79.
- Rogers, A.E.E., & Ingalls, R.P. (1969). Venus: Mapping the surface reflectivity by radar interferometry. *Science*, 165(3895), 797-799.
- Rosen, P.A., Hensley, S., Zebker, H. A., Webb, F.H., & Fielding, E.J. (1996). Surface deformation and coherence measurements of Kilauea Volcano, Hawaii, from SIR-C radar interferometry. *Journal of Geophysical Research, Planets*, 101(E10), 23109-23125.

Salora, G., De Novellis, V., Castaldo, R., De Luca, C., Lanari, R., Manunta, M., & Casu, F. (2016). Coseismic fault model of Mw 8.3 2015 Illapel earthquake (Chile) retrieved from multi-orbit Sentinel1-A DInSAR measurements. *Remote Sens*, 8(4), 323.

Şengün, Y.S. (2008). GPS ve InSAR ölçülerini birlikte kullanarak İzmit Depreminde oluşan deformasyonun modellenmesi (PhD thesis) Istanbul Technical University, Istanbul, Turkey.

Tomás, R., & Li, Z. (2017). Earth observations for geohazards: present and future challenges. *Remote Sensing*, 9(3), 194.

Vadon, H., & Sigmundsson, F. (1997). Crustal deformation from 1992 to 1995 at the Mid-Atlantic ridge, Southwest Iceland, mapped by satellite radar interferometry. *Science*, 275(5297), 193-197.

Wang, Z., Balz, T., Zhang, L., Perissin, D., & Liao, M. (2009). Using TSX/TDX pursuit monostatic SAR stacks for PS-InSAR analysis in urban areas. *Remote Sensing*, 11, 1, 26.

Yılmaztürk, S. (2015). SBAS-InSAR yöntemiyle düşey yönlü yüzey deformasyonlarının belirlenmesi: Bursa-Orhaneli linyit madeni örneği (MSc thesis) Istanbul Technical University, Istanbul, Turkey.

Url-1: <https://www.sarproz.com>, (last accessed 2 April 2018)

Url-2: <https://www.radartutorial.eu/01.basics/pic/radarprinzip.print>, (last accessed 4 November 2019)



© Author(s) 2021. This work is distributed under <https://creativecommons.org/licenses/by-sa/4.0/>